Hippocampal remapping after partial inactivation of the medial entorhinal cortex

Chenglin Miao[1], Qichen Cao[1], Hiroshi T. Ito[1], Homare Yamahachi[1], Menno P. Witter[1], May-Britt Moser[1] and Edvard I. Moser[1]

[1]Kavli Institute for Systems Neuroscience and Centre for Neural Computation, Norwegian University of Science and Technology, Trondheim, Norway;

Corresponding author: Chenglin Miao, chenglin.miao@ntnu.no; Edvard I. Moser, edvard.moser@ntnu.no

Manuscript length: 78,223 characters (with spaces included), 7 figures, 6 supplemental figures, 5 supplemental tables.

Author contributions

C.M., E.I.M. and M.-B.M designed research, C.M. and Q.C. collected data, C.M., Q.C. and H.T.I. analyzed data, M.W. helped with anatomy and histology, M.-B.M, and E.I.M. supervised the project, and C.M.,. H.T.I., Y.H. and E.I.M. wrote the paper with the input from all authors.

Acknowledgments

We thank A.M.Amundsgård, K.Haugen, A.Burøy, E.Kråkvik, H.Waade, and V.Frolov for technical assistance. We thank Karl Deisseroth, Stanford University, for providing AAV2-CamKII-eArch3.0-EYFP virus. We thank Edward Boyden, MIT, for allowing us to use the vector AAV5-CAG-ArchT-GFP and Bryan Roth, UNC, for allowing us to use AAV2-Syna-hM4D-mCitrine. The work was supported by two Advanced Investigator Grant from the European Research Council ('ENSEMBLE' – grant agreement no. 268598; GRIDCODE – grant no. 338865), a FRIPRO grant from the Research Council of Norway (grant no. 214164), the Centre of Excellence scheme of the Research Council of Norway (Centre for the Biology of Memory, grant number 145993; Centre for Neural Computation, grant number 223262), the Louis Jeantet Prize, the Körber Prize, and the Kavli Foundation.

Summary (150 w)

Hippocampal place cells undergo remapping when the environment is changed. The mechanism of hippocampal remapping remains elusive but spatially modulated cells in the medial entorhinal cortex (MEC) have been identified as a possible contributor. Using pharmacogenetic and optogenetic approaches, we tested the role of MEC cells by examining in mice whether partial inactivation in MEC shifts hippocampal activity to a different subset of place cells with different receptive fields. The pharmacologically selective designer Gi-protein-coupled muscarinic receptor hM4D or the light-responsive microbial proton pump archaerhodopsin (ArchT) was expressed in MEC, and place cells were recorded after application of the inert ligand clozapine-N-oxide (CNO) or light at an appropriate wavelength. CNO or light caused partial inactivation of the MEC. The inactivation caused substantial remapping in the hippocampus, without disrupting the spatial firing properties of individual neurons. The results point to MEC input as an element of the mechanism for remapping in place cells.

Introduction

The neuroscience of memory entered the modern era when Scoville and Milner reported, more than 50 years ago, that surgical removal of the hippocampi caused a severe disruption of memory for daily-life events (Scoville and Milner, 1957). Studies in animals and human subjects during the subsequent decades showed that the hippocampus is necessary for long-term memory of experience and facts, collectively referred to as declarative memory (Squire, 1992; Eichenbaum, 2000; Nadel et al., 2000). It is only more recently, however, that experiments have started to uncover the neural mechanisms of hippocampal memory formation.

A major advance in the search for hippocampal memory mechanisms was the discovery of place cells (O'Keefe and Dostrovsky, 1971). Place cells are cells that fire specifically when an animal is at a certain position in the environment. Different place cells fire at different positions, such that, collectively, the cells form a map-like dynamic representation of a moving animal's position (O'Keefe, 1976; O'Keefe and Nadel, 1978). However, place cells do not only represent the animal's current location. They may also reflect memory of a location, expressed as position-correlated firing patterns in the absence of the sensory inputs that originally elicited the firing (O'Keefe and Speakman, 1987; Jarosiewicz and Skaggs, 2004; Leutgeb et al., 2005), or as an influence of past or future trajectories on the firing rates of place cells within their place fields (Wood et al., 2000; Frank et al.,2000; Ferbinteanu and Shapiro, 2004; Ito et al., 2015). Expression of memory in place cells is also apparent when place cells develop associations with reward-predictive stimuli (Komorowski et al., 2009; Igarashi et al., 2014) or when

spatial firing patterns during foraging are subsequently replayed when the animal is resting (Pavlides and Winson, 1989; Wilson and McNaughton, 1994). The ability of place cells to express locations experienced in the past points to place cells as part of the mechanism for representation of experience in the hippocampus.

One indication of a link between place cells and memory is the existence of large numbers of apparently independent spatial representations, or maps, in the hippocampus (Colgin et al., 2008; Alme et al., 2014). Transitions between such representations are referred to as 'remapping' (Muller and Kubie, 1987; Muller et al., 1991). Under some conditions, place cells completely change their firing patterns in response to relatively minor alterations in sensory or motivational inputs (Muller and Kubie, 1987; Markus et all., 1995). Following changes in the configuration or location of an environment, place fields may appear, disappear or move to new locations. Under these circumstances, the new pattern of activity may be no more similar to the original pattern than expected by chance (Leutgeb et al., 2004). This nearly complete orthogonalization of hippocampal place maps for different environments ('global remapping') is thought to enable storage of discrete representations, with minimal risk of interference (Battaglia and Treves, 1998; Colgin et al., 2008).

The mechanism of hippocampal remapping has not been determined. Activity changes in the hippocampus can be elicited by a number of cortical and subcortical inputs. One of these is the projection from medial entorhinal cortex (MEC), which comprises axons from a variety of spatially modulated cell types, including grid cells and border cells (Hafting et al., 2005; Solstad et al., 2008; Zhang et al., 2013). Remapping in hippocampal place cells could reflect changes in the firing pattern of these entorhinal cell types, such as a relative displacement of the firing locations of grid cells from different grid modules when the animal moves from one environment to another (Fyhn et al., 2007; Stensola et al., 2012). In agreement with this hypothesis, inactivation of the MEC appears to cause substantial change in the firing locations of hippocampal place cells in two studies (Ormond and McNaughton, 2015, their Figure S8; Rueckemann et al., 2015), although it is not clear whether such change reflects a switch to a new map or mere instability in the firing locations of the place cells. In the one study where time course was estimated (Rueckemann et al., 2015), the change was slow and gradual, with a developmental trajectory very different from the sharp transition usually observed in response to salient changes in the environment (Muller and Kubie, 1987; Leutgeb et al., 2006). To determine the nature of the remapping, we recorded, on a lap-by-lap basis, the firing locations of place cells in hippocampal area CA3 after partial but specific inactivation of the MEC, using either virus-assisted optogenetic or pharmacogenetic techniques for local neuronal silencing. If remapping is caused by changes in the pattern of simultaneously active MEC cells, remapping should be seen with

both approaches after partial MEC inactivation. The study also gave us the opportunity to determine, with more specific interventions, the impact of MEC input on the formation of place fields in the hippocampus.

Results

Strategy for partial inactivation of the MEC

To determine whether changes in MEC firing patterns cause remapping in hippocampal place cells, we silenced MEC cells in mice with tetrodes implanted at dorsal-to-intermediate levels of the CA3 area of the hippocampus (Figure 1). MEC neurons were silenced by local injection of an adeno-associated virus (AAV) expressing either the pharmacologically selective designer Gi-coupled muscarinic receptor hM4D (Armbruster et al., 2007) or the optogenetic silencer archaerhodopsin (ArchT) (Chow et al., 2010; Han et al., 2011). hM4D was fused with the fluorescent protein mCitrine; ArchT was fused with GFP. In 14 mice, AAV was injected in both dorsal and ventral MEC in order to cover the entire dorso-ventral length of the MEC ('global MEC infection', 8 mice with hM4D and 6 mice with ArchT). In 6 mice, AAV was injected in dorsal MEC only (4 mice with hM4D and 2 mice with ArchT). In 3 mice, AAV was injected only in ventral MEC (all hM4D). In addition, 3 mice received control injections of AAV-mCitrine (n = 2) or AAV-GFP (n = 1) at dorsal and ventral MEC locations.

To verify that MEC cells can be inactivated following expression of hM4D or ArchT, we implanted tetrodes within the infected area. Three weeks post-infection, we recorded entorhinal spike activity while the mice foraged randomly in a 1 m wide square box (Figure 1A). Grid cells, border cells and head direction cells were identified based on firing patterns in the box. We then recorded the same cells in a smaller box (30 x 30 cm) to maximize coverage and to reduce recording time. In AAV-hM4D-infected animals, after 5 min baseline recording, the infected cells were hyperpolarized by i.p. injections of the hM4D-specific ligand clozapine-N-oxide (CNO) (Figure 1B). Thirty minutes later, activity in the small box was reduced to less than 50% of the baseline rate in 29 out of 35 MEC neurons. Mean firing rates were reduced from 2.36 ± 0.34 Hz before CNO to 0.71 ± 0.24 Hz 30 min after CNO (35 cells from 2 mice, Wilcoxon signed rank test, $Z = 4.82$, $P = 3.0 \times 10^{-5} < 0.0001$, Figure 1C). The activity recovered towards baseline levels after 12 h (mean firing rate, 2.02 ± 0.39 Hz, Wilcoxon signed rank test, $Z = 1.95$, $P = 0.52$). In AAV-ArchT-infected animals, the MEC cells were inactivated by continuous laser application at a wavelength of 532 nm. Firing rates were reduced to less than 50% of the baseline rate in 22 out of 24 MEC neurons. Mean rates were reduced from 1.30 ± 0.26 Hz before light application to 0.28 ± 0.11 Hz 30 min after light (24 cells from 3 mice, Wilcoxon signed rank test, $Z = 3.86$, $P = 1.0 \times 10^{-4}$, Figure 1F). All functional cell types were inhibited in both experiments (all 6 grid cells; 2 out of 3

140 border cells; 3 out of 4 and 4 out of 5 head direction cells, respectively; Figure 1A and D). mCitrine-
141 hM4D expression was not observed in hippocampal cell bodies, only in bypassing axons (10 mice; 6-
142 16sections per animal; Figure S3A to C), suggesting that the effect of CNO was largely restricted to the
143 injection area in the MEC. GFP-ArchT was seen in CA2 in 2 out of 8 mice with ArchT expression; in the
144 remaining mice, no expression was detected in cells with cell bodies in the hippocampus (Figure 3, D
145 to F).

146 To estimate the extent of MEC inactivation with a different method, we compared the number of c-
147 Fos positive cells after CNO injection on the injection side with the number on the contralateral side in
148 animals with unilateral AAV-hM4D injections. Cells were counted within randomly selected windows
149 in MEC (Figures S5). The density of c-Fos positive cells on the AAV-hM4D-infected side of MEC was
150 significantly lower than on the uninfected contralateral side (19.2 ± 4.0 % vs. 43.8 ± 11.9 % of MEC cells,
151 Mann-Whitney U test, Z = 2.19, P = 0.028). The reduction of MEC activity after local silencing validates
152 the hM4D intervention as a strategy for partial silencing of the MEC.

153 **Spatially selective firing is maintained in the hippocampus after partial MEC inactivation**

154 We first examined how individual place cells respond to changes in the pattern of simultaneously active
155 cells in the MEC. AAV-hM4D-mCitrine was injected across multiple dorso-ventral levels of MEC in 15
156 mice with tetrodes in hippocampal area CA3. In animals with both dorsal and ventral injections,
157 mCitrine-expressing cells could be observed across the entire dorso-ventral range of MEC (Figure 2A).
158 In dorsally injected animals, expression was limited to the dorsal half, whereas after ventral injections,
159 it was limited to the ventral part (Figure 2A). On average, mCitrine was expressed across 49.0 ± 17.8 %
160 of the MEC (mean ± S.E.M.; individual estimates range between 23.1% and 78.3%; Figure S1 and Table
161 S1). On average, 18.7 ± 6.6 % of the infection volume was in neighbouring regions, including lateral
162 entorhinal cortex (4.3 ± 4.0 % of the part of lateral entorhinal cortex that was present in sections
163 containing MEC; see Experimental Procedures), presubiculum (7.0 ± 6.8 % of this area), and
164 parasubiculum (12.2 ± 8.1 %), postrhinal cortex (13.0 ± 11.8 %), subiculum (2.0 ± 2.9 %), and dentate
165 gyrus (0.2 ± 0.1 %). Within the infected area, the large majority of the cells, probably more than 90%,
166 were hM4D-mCitrine positive (Figure S2, A to D).

167 Place cells were recorded from CA3 while the mice ran a minimum of 10 laps on a 1 m long linear track.
168 Running was rewarded by chocolate crumbs at the ends of the track. We restricted our analysis to cells
169 with stable location-selective activity on the baseline sessions (spatial correlation of 1st and 2nd halves
170 of the session > 0.5). 41 out of 139 cells (30%) expressed stable location selective activity at least in
171 one running direction on the track. 34 of them (24%) expressed firing fields in both running directions.
172 Because most of these cells fired at different locations on left and right runs (spatial correlation: 0.252

± 0.028; peak position difference: 15.3 ± 2.2 cm, peak rate difference [low/high]: 0.48 ± 0.04; mean ± s.e.m.), as reported previously (McNaughton et al., 1983), we treated run directions as distinct data sets (Table S2). The total number of data sets was 109.

Inactivation of MEC with the hM4D ligand CNO had minimal impact on the spatial firing properties of individual place cells in hM4D-expressing animals. There was a significant reduction of the mean firing rate of the place cells (before CNO, 3.83 ± 0.42 Hz; 30 min after CNO, 2.81 ± 0.33; Wilcoxon signed rank test $Z = 4.06$, $P = 4.9 \times 10^{-5}$) (Figure 3C) but there were no significant changes in spatial firing properties such as spatial information content (before CNO: 0.85 ± 0.06 bits/spike; 30 min after CNO, 0.83 ± 0.07 bits/spike, Wilcoxon signed rank test $Z = 0.697$, $P = 0.49$, Figure 3D) or the number of firing fields per cell (before CNO: 1.12 ± 0.03; 30 min after CNO: 1.02 ± 0.057; Wilcoxon signed rank test, $Z = 1.52$, $P = 0.127$). The size of the place fields was estimated by constructing, for all cells in the experimental group, a cross-correlation matrix of pairs of population vectors for firing rates along successive bins of the track (20 bins in total; 4 cm each; Fig. 3E to H). The mean distance from the diagonal of the matrix to population vectors with a mean correlation of 0.2 was considered as the effective size of the place fields (Ormond and McNaughton et al., 2015). Place field size was not significantly changed after CNO ($r = 0.2$ threshold before CNO: 4.65 ± 0.49 bins; 30 min after CNO: 4.80 ± 0.65 bins, $P = 0.85$; P value was estimated from bootstrap distributions) (Figure 3E to H). The lack of effect on size of place fields was threshold-independent (Fig. 3H). There was no significant change in the running speed of the animal after CNO (before: 24.2 ± 0.66 cm/s, 30 min after: 23.3 ± 0.85 cm/s, Wilcoxon signed rank test, $Z = 1.465$, $P = 0.143$).

There was only minimal difference in place field properties of mice with hM4D expression limited to either dorsal or ventral MEC. Mean firing rates were reduced significantly after CNO in the ventral injection group (before CNO, 5.70 ± 0.99 Hz; 30 min after CNO, 3.36 ± 0.62 Hz; Wilcoxon signed rank test $Z = 3.80$, $P = 1.43 \times 10^{-4}$) but not in mice with dorsal injections (before CNO, 3.41 ± 0.88 Hz; 30 min after CNO, 3.23 ± 0.67 Hz; Wilcoxon signed rank test $Z = 0.315$, $P = 0.75$). There was no change in the spatial firing properties of place fields in either group. Spatial information was unaltered (dorsal group before CNO: 1.02 ± 0.15 bits/spike; 30 min after CNO, 0.87 ± 0.13 bits/spike, Wilcoxon signed rank test $Z = 0.545$, $P = 0.586$; ventral group before CNO: 0.64 ± 0.07 bits/spike; 30 min after CNO, 0.77 ± 0.10 bits/spike, Wilcoxon signed rank test $Z = 0.898$, $P = 0.339$). There was no change in the population vector cross-correlation matrices used to determine field size (distance from diagonal in the dorsal group: before CNO: 5.14 ± 0.39 bins; 30 min after CNO: 4.90 ± 0.45 bins, $P = 0.82$; distance from the diagonal in the ventral group before CNO: 6.25 ± 0.75 bins; 30 min after CNO: 5.07 ± 0.57 bins, $P = 0.19$; P values were estimated from bootstrap distributions) (Figure 5 E and J).

206

207 **Hippocampal remapping after partial MEC inactivation**

208 CNO caused substantial remapping in the place-cell population (Figure 4 and Table S2, S3 and S5).
209 Remapping was expressed in individual place cells as a drop in spatial correlation between rate maps
210 for baseline trials and trials conducted with the same cells in the same environment 30 min after CNO
211 (first vs. second half of the baseline: $r = 0.76 \pm 0.013$; 30 min after CNO vs. baseline: $r = 0.41 \pm 0.045$,
212 paired sample t test after Fisher z-transformation, $t(108) = 6.41$, $P = 4.08 \times 10^{-9}$). The spatial correlation
213 was still reduced 12 h after CNO (12 h after vs. baseline: 0.46 ± 0.038, paired sample t test $t(108) =$
214 7.17, $P = 9.84 \times 10^{-11}$), although the firing fields at 12 h correlated more strongly with the baseline
215 pattern than with the pattern 30 min after CNO ($r = 0.36 \pm 0.038$; paired sample t test after Fisher z-
216 transformation, $t(108) = 2.41$, $P = 0.018$). For cells expressing place fields in both running directions,
217 the amount of remapping, measured by spatial correation between baseline and the CNO trial, was
218 positively correlated between inbound and outbound place fields ($R = 0.616$, $P = 0.002$). A similar drop
219 in correlation during CNO was not present in AAV-GFP-infected control mice, despite widespread GFP
220 expression (mean correlation: 0.77 ± 0.03, $n = 18$; two-sample t test $t(125) = 2.88$, $P = 0.005$, Figure
221 4B). The drop in spatial correlations after CNO injection in the hM4D group was accompanied by a
222 significant shift of the center of mass of the place fields compared to the first vs. second half of the
223 baseline session (mean ± s.e.m.: 12.8 ± 1.4 cm vs. 5.5 ± 0.72 cm; Wilcoxon signed rank test, $Z = 4.869$,
224 $P = 1.0 \times 10^{-6}$).

225 The distribution of spatial correlations between firing before and after CNO was compared to a
226 shuffled distribution obtained by random displacement of firing locations along the trajectory on the
227 track of the animal together with random replacement of cell identities. The spatial correlation
228 between the first half and the second half of the baseline session, before CNO, was significantly above
229 the 95th percentile of the shuffled distribution for 101 out of 109 sets of place fields (94%) (Figure 4B),
230 as expected given that cells were pre-selected for stability. After CNO application, the correlation with
231 the baseline session dropped. Only 55 out of the 109 place fields (51%) had spatial correlation values
232 that passed the 95th percentile of the shuffled distribution (baseline vs. CNO, $Z = 6.99$, $P = 2.79 \times 10^{-12}$;
233 binomial test). The low similarly to the baseline pattern was maintained 12 h after CNO (55 place fields,
234 or 51%, above the 95th percentile). A similar reduction was seen at 12 h in control animals (12 out of
235 18 place fields, or 67%; CNO vs. control, binomial test, $Z = 1.27$, $P = 0.20$, Figure 4B), as expected given
236 the low long-term stability of place fields in mice (Kentros et al., 2004).

237 At the neural ensemble level, there was a significant reduction after CNO in correlations between
238 population vectors across bins of the linear track (bin size 4 cm, 20 bins in total; Figure 4B). Before

CNO, all 20 population vector correlations were outside of the 95th percentile of a shuffled distribution (first vs. second half of the baseline session). After CNO, only 14 correlations (70%) passed the 95th percentile threshold ($Z = 2.66$, $P = 0.008$, binomial test compared to the baseline). The shift persisted 12 h after CNO (16 correlations, or 80%, above the threshold). In control mice infected with AAV-GFP, all 20 correlations exceeded the 95th percentile threshold at 30 min, which is significantly above the level in the hM4D group ($Z = 2.66$, $P = 0.008$, binomial test). At 12 h, the number had dropped to 14 (70%). In agreement with these counts, the drop in population vector correlations at 30 min in the hM4D group was significantly larger than in the control group (mean correlations of 0.18 ± 0.02 and 0.74 ± 0.04, respectively; t test for correlation values after Fisher z-transformation, $t(38) = 9.49$, $P = 1.43 \times 10^{-11}$, Figure 4B). Taken together, the results show that partial inhibition of the MEC induces substantial change in the firing locations of place cell ensembles in the hippocampus.

The decrease in spatial correlations was observed also in the subgroup of animals with inactivation limited to the dorsal MEC (Figure 5A and S1; first vs. second half of the baseline: 24 out of 30 place fields passed the 95th percentile threshold; mean correlation value: 0.77 ± 0.028; 30 min after CNO vs. baseline: 16 out of 30 fields passed the threshold; mean correlation: 0.50 ± 0.08, binomial test, $Z = 2.19$, $P = 0.03$; paired sample t test for correlation values after Fisher z-transformation, $t(29) = 3.04$, $P = 0.005$). There was a small decrease in spatial correlation also after ventral MEC inactivation (first vs. second half of the baseline: 25 out of 28 place fields passed the 95th percentile threshold; mean correlation value: 0.79 ± 0.022; 30 min after CNO vs. baseline: 20 out of 28 fields passed the threshold; mean correlation: 0.64 ± 0.06, binomial test, $Z = 1.68$, $P = 0.09$; paired sample t test for correlation values after Fisher z-transformation, $t(27) = 2.30$, $P = 0.03$). In the population vector analyses, there was a significant decrease in the number of bins passing the 95th percentile of the shuffled distribution 30 min after CNO in the dorsal hM4D group (before CNO 20/20 bins; after CNO: 5 bins; binomial test, $Z = 4.89$, $P = 9.63 \times 10^{-7}$; Figure 5D). A similar reduction was not observed in mice with selective ventral MEC inhibition (before CNO: 20/20 bins; after CNO:19/20 bins; binomial test, $Z = 1.01$, $P = 0.31$; Figure 5I).

We next asked whether the change in spatial firing patterns after CNO was instantaneous, as expected if a new ensemble pattern was recruited in the same way as when place cells remap in a novel environment. Alternatively, firing patterns might change gradually, as would be expected if the change was caused by instability in the hippocampal ensemble code (Kentros et al., 2004). To distinguish between these possibilities, we compared population vectors on each lap with the average of the baseline session. Because each session consisted of 10 laps or more, we selected the last 10 laps from the baseline session and the first 10 laps from the CNO session. In hM4D mice, we found that the population vector correlation with the baseline average was significantly lower on the first lap after

CNO (the 11th lap) than on the last lap before CNO (Figure 6A; before: 0.47 ± 0.02; after: 0.22 ± 0.03, t test for correlation values after Fisher z-transformation, $t(38) = 6.93$, $P = 3.11 \times 10^{-8}$). The correlation between the 11th lap and the average of the first 10 laps after CNO was significantly higher than the correlation with the average of the 10 preceding baseline laps (0.47 ± 0.02 vs. 0.30 ± 0.02, t test for correlation values after Fisher z-transformation, $t(38) = 4.89$, $P = 1.86 \times 10^{-5}$) (Figure 6 A). A similarly sudden drop on the first lap after CNO was not observed in GFP control animals (Figure 6B). The abrupt change of the population vector correlation suggests that the place-cell population remapped instantaneously.

Remapping after targeted inhibition of MEC projections

The pharmacogenetic study points to MEC, and particularly dorsal MEC, as a critical source of remapping in dorsal hippocampal place cells. To determine if this influence is mediated by direct projections from MEC cells to the hippocampus, we used optogenetic methods to selectively inactivate MEC fibers within the hippocampus itself. ArchT-encoding AAV was infused in MEC and place cells were recorded in CA3, at the same septotemporal level as in the pharmacogenetic study, while continuous 532 nm laser light was applied through an optic fiber aimed at the perforant path (Figure S1, Figure 7A). ArchT-GFP was expressed across 53.6 ± 11.9% of the MEC (mean ± S.E.M.; individual estimates range between 35.3% and 70.4%; Figure S1 and Table S1). Only 20.7 ± 7.5 % of infected volume was outside the MEC (4.2 ± 3.6% of the lateral entorhinal cortex that was part of sections comprising MEC, see experimental procedures; 5.3 ± 4.5% of presubiculum, 14.0 ± 6.0% of parasubiculum, 9.1 ± 5.5% of postrhinal cortex and 3.8 ± 4.8% of subiculum). Within the infected area, a large majority of the cells, probably over 90%, were ArchT-GFP positive (Figure S2, E to H). The effect of ArchT-induced silencing was expressed in all types of spatial cells in the MEC, including grid cells, head direction cells and non-classified spatial cells (Figure 1D-F). Continuous laser illumination (3 to 5 min) in the hippocampus did not induce neural apoptosis at levels that were detectable in a TUNEL assay (Figure S3, G to I).

In the 8 animals with ArchT expression in MEC, 56 out of 109 CA3 cells expressed stable location-selective activity on the track in the baseline session. 83 sets of stable place fields were obtained after combining run directions. The laser stimulation decreased the mean firing rate of place cells in CA3 (before laser, 3.18 ± 0.44 Hz; with laser, 2.31 ± 0.30 Hz; Wilcoxon signed rank test, $Z = 2.06$, $P = 0.04$; Figure 7C). The rates in the ArchT group recovered only partially when the light was terminated (2.54 ± 0.40 Hz 5-20 min after termination of the stimulation; Wilcoxon signed rank test, $Z = 2.92$, $P = 0.004$). There was no significant reduction of firing rate in GFP control mice (before laser, 2.83 ± 0.90 Hz; with

laser, 2.68 ± 0.82 Hz; Wilcoxon signed rank test, Z = 0.672, P = 0.50), suggesting that the rate reduction was not due to stimulation-induced tissue dysfunction. Laser stimulation caused a significant decrease in spatial information in place cells (before laser, 1.02 ± 0.06 bits/spike; with laser, 0.74 ± 0.06 bits/spike, Wilcoxon signed rank test, Z = 4.32, P = 1.5×10^{-5}, Figure 7C). There was no significant change in the size of the place fields as determined by population vector cross-correlation analysis (mean distance from diagonal to r = 0.2 threshold before laser, 3.41 ± 0.49 bins; with laser, 4.00 ± 0.35 bins, P = 0.50; P value was estimated from bootstrap distributions). There was also no change in the number of place fields (1.18 ± 0.05 vs. 1.22 ± 0.07; Wilcoxon signed rank test, Z = 0.435, P = 0.664).

Laser illumination led to a significant drop in spatial correlation between baseline and test trial comparable to the drop observed in animals with AAV-hM4D injections in the MEC (Figure 4 and Table S2, Table S3). For cells that expressed place fields in both running directions, the amount of remapping, during laser application, was positively correlated between inbound and outbound place fields (R = 0.544, P = 0.0023), mirroring the results from the hM4D experiment. During the baseline trial, the rate maps were stable. In 75 out of 83 place fields (90%), the spatial correlation between the first half and the second half of the baseline session exceeded the 95th percentile of a shuffled distribution (Figure 7E). With laser application, only 30 of the 83 place fields (35%) passed the threshold (Z = 7.25, P = 4.34×10^{-13} , binomial test). 44 out of 83 place fields passed the threshold after termination of the laser stimulation. The decrease in the spatial correlation during laser illumination was significant (with laser vs. baseline: r = 0.31 ± 0.051; first vs. second half of the baseline: r = 0.81 ± 0.014, paired sample t test for correlation values after Fisher z-transformation, t(82) = 9.37, P = 1.06×10^{-14}). The spatial correlation with baseline showed some recovery after termination of the laser illumination (0.52 ± 0.05, paired sample t test for correlation values after Fisher z-transformation compared with laser sessiont(82) = 4.73, P = 9.00×10^{-6}). The drop in spatial correlations in the ArchT group was accompanied by a significant shift of the center of mass of place fields compared to the first vs. second half of the baseline session (13.4 ± 1.4 cm vs. 7.3 ± 1.6 cm; Wilcoxon signed rank test, Z = 4.03, P = 5.6×10^{-5}), as well as a drop in the population vector correlations. Whereas 20 out of 20 bins (100%) of the population vector correlations were outside of the 95th percentile of the shuffled distribution for the first vs. the second half of the baseline trial, the number dropped to 15 (75%) for the comparison of light application and baseline (Z = 2.39, P = 0.017, binomial test) (Figure 7E). The drop in the population vector correlations in the ArchT group was not significantly different from the drop with hM4D-mediated MEC inactivation (30 min post-CNO; 0.18 ± 0.02 vs. 0.21 ± 0.034, respectively; t(38) = 0.85, P = 0.398) but the decrease was significantly larger than when the light stimulation was applied in GFP control mice (0.87 ± 0.10; t(38) = 6.19, P = 3.11×10^{-7}). Taken together, these results show that inactivation of dorsal MEC axons induces strong remapping in CA3 place cells.

As in the hM4D group, the change in spatial firing during laser stimulation was instantaneous. Population vectors were defined for each bin of each lap and correlated with the average vectors of the baseline session (Figure 6). We selected the last 10 laps from the baseline session and the first 10 laps from the laser session. The population vector correlation with the baseline average was significantly lower on the first lap after laser onset than on the last lap before the laser was turned on (before: 0.55 ± 0.031; after: 0.12 ± 0.053, t test for correlation values after Fisher z-transformation, $t(38) = 6.94$, $P = 2.94 \times 10^{-8}$). The correlation between the first lap with laser and the average of the first 10 laps with the laser was significantly higher than the correlation between the first lap with laser and the average of the 10 baseline laps (0.53 ± 0.020 vs. 0.25 ± 0.024, t test for correlation values after Fisher z-transformation, $t(38) = 8.85$, $P = 9.10 \times 10^{-11}$) (Figure 6 C). Abrupt changes in firing patterns were not observed in GFP control animals with laser illumination (Figure 6D). The sudden transition of the population vector correlation on the first lap after laser onset is consistent with instantaneous remapping in the place-cell population.

Finally, remapping was not caused by retrograde transport of AAV to hippocampal neurons, since in 6 out of 8 mice there was no retrograde expression of ArchT in the hippocampus (Figure S3D to F). Although GFP-ArchT was seen in CA2 in 2 animals (Figure S4, E to H, exclusion of these animals did not abolilsh the drop in spatial correlations after light application (1^{st} vs. 2^{nd} half of baseline: 0.81 ± 0.02; laser vs. baseline: 0.25 ± 0.05, t test for correlation values after Fisher z-transformation, $t(70) = 10.2$, $P = 1.96 \times 10^{-15}$; PV correlation of 1^{st} vs. 2^{nd} half of baseline: 0.72 ± 0.03; PV correlation with laser vs. baseline: 0.18 ± 0.04, t test for correlation values after Fisher z-transformation, $t(38) = 11.0$, $P = 2.39 \times 10^{-13}$) (Figure S7).

Discussion

This study reports two sets of observations. First, hippocampal place cells maintain their localized firing pattern after partial inactivation of the MEC. hM4D and ArchT were expressed across widespread regions of MEC, covering most of its dorsolateral and mediolateral extent, but the intervention caused only minor changes in the size and shape of firing fields of place cells in the CA3 of the hippocampus. Second, while spatial firing was maintained, the distribution of firing locations was altered even after quite restricted silencing in the dorsal parts of MEC. Partial MEC inactivation caused substantial

changes in hippocampal spatial representation at the neural ensemble level, reminiscent of the global remapping that occurs in place cells when animals move from one environment to another.

These findings have implications for the mechanisms of place-cell formation. The persistence of spatial firing despite widespread reduction in the firing rates of MEC neurons is consistent with results showing that a certain degree of localized firing is maintained in CA1 of animals with extensive bilateral lesions of the MEC, although the remaining firing fields are unstable (Miller and Best, 1980; Hales et al., 2014; Schlesiger et al., 2015). In the present study, MEC activity was decreased both instantaneously and reversibly, suggesting that the residual spatial firing was not caused by sprouting or other types of long-term compensatory reorganization known to take place in the hippocampus following entorhinal damage (Deller and Frotscher, 1997). The observations imply that localized firing can be generated in place cells by inputs from a wide range of afferent neurons, such that when a fraction, or even the majority, of these inputs is silenced, other spatial inputs may take over as determinants of firing locations in place cells. Following partial MEC inactivation, place fields may be generated by inputs from MEC cells whose firing rates were only partly reduced, or from spatially modulated cells in other parahippocampal regions including the parasubiculum and the lateral entorhinal cortex (Hargreaves et al., 2005; Boccara et al., 2010) .

Place fields may receive spatial information from a variety of cell types but the most prominent candidates in MEC are grid cells, border cells and head direction cells (Hafting et al., 2005; Sargolini et al., 2006; Solstad et al., 2006), which each project to the hippocampus (Zhang et al., 2013). Two classes of models have been proposed for the transformation of information from these spatial cell types to place cells in the hippocampus. In the first class, place cells are formed by summation of inputs from either grid cells across a range of spatial frequencies (Fuhs and Touretzky, 2006; McNaughton et al., 2006; Solstad et al., 2006) or from border cells with variable distances from local borders in the environment (O'Keefe and Burgess, 1996; Hartley et al., 2000). This class of models requires a quite specific connection regime. In the second class of models, connections are largely random and different place cells receive, on average, more or less the same mix of inputs, with spatial selectivity arising only in the hippocampus itself, either by local circuit computation (Monaco and Abbott, 2011; De Almeida et al., 2012) or via Hebbian plasticity (Rolls et al., 2006; Si and Treves, 2009; Savelli and Knierim, 2010). The present results show that place cells continue to fire at specific locations even after considerable changes in the balance of entorhinal inputs. There was no systematic change in the size of hippocampal place fields, contrary to predictions of simple versions of the linear summation model for place field formation from grid cells. A similar lack of change in size of firing fields was apparent in another study that inactivated MEC cells with optogenetic methods (Rueckemann et al., 2015). Other studies using less confined inactivation methods have found a contraction of fields following large

dorsal entorhinal lesions that extend into ventral entorhinal cortex (Van Cauter et al., 2008), or an expansion of fields following either dorsal or ventral entorhinal inactivation (Ormond and McNaughton, 2015) or selective lesions of layer III of MEC (Brun et al., 2008). The lesion or inactivation was more extensive and less specific in these latter studies than in the present one. With the lack of substantial and consistent changes in field size after regionally specific MEC inactivation, the present data, together with earlier and less specific work, speak in favor of an important intrahippocampal contribution to the refinement of spatial receptive fields. However, the detailed circuits and mechanisms, and the contribution of the various parahippocampal inputs, remain to be determined.

The most important finding of the present study is perhaps the observation that place cells remapped almost instantaneously after a change in the composition of MEC inputs to the hippocampus, caused by partial silencing in the MEC population. A similar shift in the distribution of place fields was observed when MEC was inactivated by local infusion of muscimol (Ormond and McNaughton, 2015; their Figure S8), although it was not clear from this study that the shift was instantaneous. In another study (Rueckemann et al., 2015), MEC cells were silenced optogenetically, but here the change in firing pattern was slow and gradual, not as expected if the mechanism was the same as when place cells remap under natural conditions (Muller and Kubie, 1987; Leutgeb et al., 2006). In the present work, the transition to a new map was fully expressed already on the first lap of running. Moreover, the new firing pattern was maintained during the inactivation session, in the same way that firing remains stable following remapping after exposure to a new environment. While the cells maintained their ability to fire at specific locations, the distribution of firing rates and firing locations was altered to the extent that correlations with the original activity pattern overlapped considerably with that of a shuffled distribution, although the orthogonalization was not complete. A possible explanation of the different remapping patterns of the two studies is the recording location. Rueckemann et al. (2015) recorded in CA1, where cells are known to exhibit considerable hysteresis across successive experimental trials (Leutgeb et al., 2005) The fast remapping observed in CA3 in the present work suggests that MEC inactivation can reproduce firing patterns of place cells that occur naturally in response to changes in MEC input when the environment is altered.

How the distribution of place fields is affected by signals from the MEC remains to be determined but the strong component of grid-cell input in the perforant-path projection to the hippocampus (Zhang et al., 2013) points to changes in firing patterns among grid cells as a major source of hippocampal remapping. Remapping may take place in the hippocampus in response to differential translations and rotations of firing maps across modules of grid cells (Fyhn et al., 2007; Stensola et al., 2012). When changes in the environment cause unequal changes in phase and orientation over grid modules, place cells will receive input from new combinations of co-active grid cells. This in turn will change both the

subset of place cells that pass the activation threshold and the location at which they are maximally activated (Stensola et al., 2012; Rowland and Moser, 2014). Determining the entorhinal firing patterns that cause remapping will eventually require interventions that target functional cell types specifically.

Experimental Procedures

Subjects. The data were obtained from 26 male mice. The mice were 22 – 35 g at implantation. They were housed separately in transparent Plexiglass cages (35 cm × 30 cm × 30 cm) in a humidity- and temperature-controlled environment. All mice had tetrodes implanted in the right hippocampus or MEC. In two of the animals, tetrodes were implanted simultaneously in the hippocampus and the ipsilateral MEC. All animals were kept at 90% of free-feeding body weight and maintained on a 12-h light/ 12-h dark schedule. Testing occurred in the dark phase.

Virus with AAV5-CAG-ArchT-GFP, AAV2-hSyn-hM4D-mcitrine, AAV5-CAG-GFP and AAV5-CAG-Tdtomato were from the University of North Carolina at Chapel Hill (UNC)'s gene therapy center. The titer of the virus was 10^{12} viral genomic particles/ ml. AAV5-CAG-ArchT-GFP and AAV5-CAG-GFP were from Edward Boyden's lab, Massachusetts Institute of Technology (MIT); AAV2-hSyn-hM4D-mcitrine was from Bryan Roth's lab, University of North Carolina at Chapel Hill (UNC). AAV2-CamKII-eArch3.0-EYFP was from Karl Deisseroth's lab, Stanford University. The titer of this virus was 10^{13} viral genomic particles/ ml.

Eight mice received injections of AAV2-CAG-ArchT-GFP, fifteen mice received injections of AAV2-Syna-hM4D-mcitrine, and two mice received injection ofAAV2-CamKII-eArch3.0-EYFP. Testing of control animals (2 mice for the hM4D group and 1 for the ArchT group) was interleaved with testing of experimental groups. The experimenter was not blind to the identity of the animals.

Surgery, virus injection and electrode preparation. All animals were anesthetized with isoflurane (air flow: 0.8 – 1.0 L/min, 0.5 – 3% isoflurane, adjusted according to physiological condition). The mice received subcutaneous injections of Bupivacaine (Marcaine) and buprenorphine (Temgesic) at the start of the surgery. Isoflurane was gradually reduced from 3% to 1%. Depth of anesthesia was examined by testing tail and pinch reflexes as well as breathing.

Upon induction of anaesthesia, the animal was fixed in a Kopf stereotaxic frame for implantation. Holes for tetrode implantation were drilled in the skull above the right hippocampus and tetrodes were then implanted. The tetrodes were made of 17 μm polyimide-coated platinum-iridium (90% -

10%) wire. The electrode tips were plated with platinum to reduce electrode impedances to around 100–250 kΩ at 1 Hz. 22 mice received a microdrive (Axona, London, U.K.) with 2 tetrodes. The tetrodes were inserted in the cortical surface 1.5-2.3 mm behind the bregma and 1.4-2.5 mm lateral to the midline. Four mice were implanted with a VersaDrive-4 (Neuralynx, Dublin, Ireland) with 4 tetrodes. The base of the VersaDrive-4 was modified to separate the tetrodes into two groups targeting MEC and hippocampus simultaneously. In the first group, two tetrodes were aimed at the right hippocampus (AP 1.5-2.3, ML 1.4-2.5) and in the second group two tetrodes were implanted above the ipsilateral MEC (0.35-0.40 mm anterior of the transverse sinus, 3.2 –3.5 mm from midline, 1.5 mm below dura, 5 degree angle in the sagittal plane, with electrode tips pointing in the posterior direction). In ArchT-expressing animals, an optic fiber (lot number: MFC_240/250-0.63_16mm_ZF1.25_FLT, Doric, Canada) was implanted in the performant-path termination zone in the hippocampus (AP 1.5-2.3, ML 1.4-2.5). Microdrives and optic fiber were secured to the skull with jewellers' screws and dental cement. Two front screws in the skull behind the eyes were connected to ground.

During the surgery, before the tetrodes were inserted, a 10-µl NanoFil syringe (World Precision Instruments, Sarasota, Florida, USA) and a 33-gauge beveled metal needle was used for virus injection in MEC (0.4–0.35 mm anterior of the transverse sinus, 3.2 –3.5 mm from midline, 1.2 mm below dura for dorsal injections, 2.5 mm below dura for ventral infections). Injection volume (0.5 to 1 µl at each location) and flow rate (0.1 µl/min) were controlled with a Micro4 Microsyringe Pump Controller (World Precision Instruments). After injection, the needle was left in place for 10 minutes before it was withdrawn slowly.

***Electrode turning and recording procedures*.** Turning of tetrodes started 2 to 3 days after the surgery. Data collection began within 2 weeks. Before each recording session, the mice rested on a towel in a large flower pot on a pedestal. The mouse was connected to the recording equipment via AC-coupled unity-gain operational amplifiers close to the head and a counterbalanced cable that allowed the animal to move freely. Over the course of 20 to 30 days, the tetrodes were lowered in steps of 50 µm or less, until well-separated single neurons could be recorded. When the signal amplitudes exceeded four times the noise level (20 to 30 µV), and single units were stable for more than 1 h, data were collected.

Recorded signals were amplified 8000 to 25,000 times and band-pass filtered between 0.8 and 6.7 kHz. Triggered spikes were stored to disk at 48 kHz (50 samples per waveform, 8 bits/sample) with a 32-bit time stamp (clock rate at 96 kHz). Electroencephalograms (EEG) were recorded single-ended from one of the electrodes. The local field potential was amplified 3000 to 10,000 times, low pass–

filtered at 500 Hz, sampled at 4800 Hz, and stored with the unit data. Through a video camera, the recording system obtained the position of two light-emitting diodes (LEDs) on the headstage of the mouse. The LEDs were tracked individually at a rate of 50 Hz. The two LEDs were separated by 4 cm and aligned with the body axis of the mice.

Over the course of 3 to 6 weeks following surgery, the mice were first trained to run in a 1m square black aluminum enclosure polarized by a white cue card. In mice with putative border cells, the session in the square box was succeeded by a test in the same box with a 50 cm long and 50 cm high wall insert in the center of the box. These trials were 15 min. In parallel with training in the box, all mice were trained to run on a 1 m long linear track. Running was motivated by randomly scattering crumbs of chocolate at 10- to 15-s intervals in the recording enclosure and by placing crumbs on alternating sides of the linear track before the conclusion of each lap. Each session lasted 10 to 15 min. On the linear track, the mice first ran 10 full laps (back and forth). In hM4d-expressing mice, this was followed by i.p. injection of 2 to 3 mg/kg of clozapine-N-oxide (CNO, Sigma). Thirty minutes later, the mice ran another 10 laps. A third session of 10 laps was conducted 12 h after the injection. In ArchT-expressing mice, the baseline session was followed by 10 trials of continuous laser stimulation (532nm) at a power density of 20 mW/mm^2 at the fiber tip. Five to 20 minutes after the laser was turned off, another 10 trials were conducted. There was no change in the running speed of the animals after laser stimulation (before: 21.2 ± 0.81 cm/s; with laser: 21.6 ± 0.79 cm/s, Wilcoxon signed rank test, Z = 0.013, P = 0.99). No signs of cell demage were seen in hippocampus after laser illumination (Figure S3, G to I).

***Spike sorting and analysis of place fields*.** Spike sorting was performed offline using graphical cluster-cutting software (Tint, Neil Burgess and Axona Ltd.). Clustering was performed manually in two-dimensional projections of the multidimensional parameter space (waveform amplitudes and waveform energies), using autocorrelation and crosscorrelation functions as additional tools and criteria. Putative interneurons were defined as neurons with a peak-to-trough spike width of less than 450 μs and mean firing rate higher than 15Hz (e.g. Bartho et al., 2004). These cells were excluded from further analysis. A segment of 10 cm was excluded from each end of the linear track for analysis. Spikes were analyzed only during the period when the animals' running speed exceeded 3 cm/s. For experiments on the linear track, instantaneous firing rates on individual laps were estimated using a Gaussian kernel on the spike data for temporal smoothing:

534 $$r(t) = \sum_{i=1}^{N} g(\frac{t_i - t}{h})$$

535 where *g* is a 1D Gaussian kernel, *h* is a bandwidth, *N* is the total number of spikes, and t_i is the time
536 of the *i*-th spike. The bandwidth was set at 100 ms. Due to minimal coverage per bin, temporal
537 smoothing gives more robust rate estimates compared to those based on spatial bins during fast
538 running on the track. Spike rate at each track position (1 cm bin) on each lap was estimated using a
539 linear interpolation method applied to the temporally-smoothed spike rates. Because the same cells
540 often had different firing fields on left and right runs, firing fields of the same cell in each run direction
541 were analyzed as two distinct data sets.

542 Place fields were analysed in cells with mean firing rates above 0.10 Hz. Cells without consistent
543 location-selective firing across laps in the baseline sessions (spatial correlation of 1st and 2nd halves
544 of the baseline session < 0.5) were also excluded. A place field was defined as a contiguous region of
545 at least 3 cm where the firing rate exceeded 50 % of the peak rate. Additional place fields were
546 counted only when the peak position of the field was separated from other fields by more than the
547 width of the field size.

548 Spatial information content in bits per spike was calculated as follows;

549 information content = $\sum_i p_i \frac{\lambda_i}{\lambda} \log_2 \frac{\lambda_i}{\lambda}$

550 where λ_i is the mean firing rate of a unit in the *i*-th bin, λ is the overall mean firing rate, and p_i is
551 the probability of the animal being in the *i*-th bin (occupancy in the *i*-th bin / total recording
552 time)(Skaggs et al., 1996).

553 Spatial correlation was obtained by calculating the Pearson correlation coefficient for mean firing
554 rates across 1 cm wide bins on of the track on a pair of sessions. For population vector analysis,
555 population vectors were defined for each 4-cm bin of rate maps (20 bins in total) from all cells in the
556 experimental group. To maintain independence of neighboring spatial bins, we estimated mean firing
557 rates in spatial bins without smoothing. For lap-by-lap population vector analyses, a total of 10 laps
558 (defined as pairs of forward and backward runs) were taken from each recording session. When the
559 sessions had more than 10 laps, we selected the 10 last laps from the baseline session, and the 10
560 first laps in the sessions with MEC inhibition. Population vector correlations were determined for
561 each spatial bin of each lap. The vectors were correlated with the 10-lap average of either the
562 baseline session or the inactivation session. Chance levels were determined by calculating spatial

correlation and population vector correlation for shuffled ensembles of place cell activity. The shuffled ensembles were generated by random replacement of cell identities as well as random displacement of firing location along the track in order to obtain place cell ensembles with different field locations as well as firing rates. This procedure was repeated 1000 times to obtain a statistical distribution of chance levels.

To convert Pearson's correlation values to more normally distributed variables, Fisher's z-transformation was performed as follows:

$$z = \frac{1}{2}\ln\left(\frac{1+r}{1-r}\right)$$

r is Pearson's correlation coefficient.In the open field, the position data were smoothed and sorted into 5 cm × 5 cm bins, and firing rate distributions were then determined by summing the total number of spikes in a given spatial bin, dividing by the amount of time that the animal spent in that bin, and smoothing with a 2D Gaussian kernel with a bandwidth of 2 bins. The data in the open field were used to determine if cells recorded in MEC satisfied criteria for grid cells, border cells, or head direction cells (Langston et al., 2010).

***Histological procedures and electrode positions*.** The mice received an overdose of Equithesin and were perfused intracardially with saline followed by either 4% formaldehyde or 4% freshly depolymerized paraformaldehyde in phosphate buffer(PFA). The brains were extracted and stored in the same fixative, and frozen sagittal sections (30 µm) were cut and stained with cresyl violet. Each section through the relevant part of the hippocampus or MEC was collected for analysis. For LEC, only parts adjacent to MEC, i.e. the parts of LEC present in sections containing MEC, were collected and analyzed. All tetrodes were identified and the tip of each electrode was found by comparison with adjacent sections. Recordings from hippocampal tetrodes were included in the data analysis if the deepest position was in the CA3 pyramidal cell layer. The electrodes were not moved after recording.

For immunostaining, sections were rinsed 3 times for 10 min in 1 × phosphate buffer (PBS; pH 7.6) at room temperature, preincubated for 2 hours in 10% normal goat serum in PBST (1 × PBS with 0.5% Triton X-100). Between incubation steps, sections were rinsed in PBST. Sections were incubated either with antibodies against NeuN, raised in donkey (Millipore, 1:500), or GFP, raised in goat (Clontech, 1:2000), or c-Fos, raised in goat (Calbiochem, 1:2000), for 72 hours in antibody-blocking buffer at 4°C. After three times of 15-min washing in PBST at room temperature, sections were incubated either in a mouse-anti donkey antibody or a rabbit-anti goat antibody conjugated with either fluorescein isothiocyanate or Cy3 (Jackson ImmunoResearch, West Grove, Pennsylvania, USA, 1:2000) for 2 hours at room temperature. After rinsing in PBS, sections were mounted onto glass

595 slides with 4',6'-diamidino-2-phenylindole (DAPI)–containing Vectashield mounting medium (Vector
596 Laboratories, Burlingame, California, USA), and a cover slip was applied. Expression of hM4D or ArchT
597 was estimated with anti-GFP, since a mCitrine or GFP tag was fused with hM4D or ArchT in the viral
598 construct (GFP antibody also specifically binds with mCitrine). NeuN was used for staining neurons.

599 To examine the inhibition in mice injected with AAV-hM4D, we stained for the expression of the
600 immediate early gen c-fos. Animals were euthanized and perfused with cold PBS and 4% PFA, 30 min
601 after injection of CNO. Sections for c-fos staining were acquired from 3 mice expressing AAV-hM4D
602 and stained as described above. The number of c-fos positive cells was determined with Image-Pro
603 Plus® software (Media Cybernetics, Silvery Spring, MD, USA). In each image, 5 of the 1 mm × 1 mm
604 size windows were randomly selected to quantify the percentage of c-fos positive cells that passed
605 the threshold in MEC. The non-infected side was used as a control. Image-Pro Plus® software was
606 used for automatic counting of count c-fos positive cells based on background optical density. Cells
607 that surpassed 2 × the background optic density were considered c-fos positive. The background optic
608 density was established for each section in a nearby region lacking c-Fos.

609 To check for potential cell damage resulting from laser illumination, we used the TdT-mediated dUTP
610 nick end labelling (TUNEL) assay. Two mice were anesthetized and perfused and brains were
611 dissected out and post-fixed for 24hrs in 4% PFA. The brains were cut and 20 µm wide sections which
612 were stored in PBS. The sections were mounted on poly-L-lysine (Sigma) coated slides, rehydrated
613 by sequential incubations in 100%, 100%, 90%, 80%, 70% ethanol lasting 2 min each. The sections
614 were then washed in 0.85% NaCl and PBS for 5 min each. Sections were fixed with 4% fresh PFA for
615 15 min and washed 3 times with PBS for 5 min each. The tissue was digested with 20 µg/ml Proteinase
616 K (Amresco) solution for 10 min, washed with PBS, and then fixed with 4% PFA for 5 min, after which
617 it was washed in PBS. For positive and negative control slides (from Abcam), cells were centrifuged
618 and pipetted onto coated slides. The cells were fixed in 4% PFA when the slides were dry and washed
619 three times in PBS, followed by 0.2% Triton X-100 (Sigma) solution for 5 min, after which they were
620 washed in PBS. Apoptotic cells were detected using an in situ BrdU-Red DNA fragmentation (TUNEL)
621 assay kit (Abcam) following the recommended standard protocol. The nuclei were labelled with
622 Hoechst (Sigma) before mounting the sections with ProLong Gold Antifade solution (Invitrogen). The
623 sections were imaged with a confocal microscope (Zeiss LSM 510).

624 ***Area of virus infection*** **and** ***unfolded maps*****.** Unfoldings of MEC were prepared by mapping, for each
625 sagittal brain section, the dorsal border of MEC onto a straight line. For each section, the surface
626 length of MEC was measured with Image-Pro Plus® software and subsequently mapped onto a
627 straight line perpendicular to the line that represents the dorsal border. In order to assess the spread

of the virus infection into areas adjacent to MEC, we also prepared unfolded maps of the postrhinal cortex, parasubiculum, presubiculum, lateral entorhinal cortex, and subiculum. In the case of postrhinal cortex, we used as a reference the ventral border, either with MEC or parasubiculum. For para- and presubiculum, the respective borders with MEC and subiculum were used. The lateral entorhinal cortex was aligned using its border with MEC, while for the subiculum, we used the border with CA1 as the alignment point in the map. Dorsal and ventral parts of the subiculum and of the pre- and parasubiculum were merged in these unfoldings. All borders were established using cytoarchitectonic criteria that can reliably be established irrespective of the plane of sectioning, as described in detail for the rat brain (Boccara et al, 2015). These borders, as defined in the rat, can be realibly applied to the mouse brain (Witter 2012). It is important to point out that in particular the mediolateal extent of parasubiculum, as wel as that of postrhinal cortex, is extremely variable between individual animals. Cytoarchitectonic criteria, correlated to established chemoarchitectonic criteria, are therefore the only realiable way to establish those borders (Boccara et al., 2010; Boccara et al 2015). The percentage of the infected area on the unfolded map was taken as an indicator of the spread of hM4D or ArchT expression. Images of entorhinal cortex were scanned with an automated scanner (MIRAX MIDI, Carl Zeiss, Germany). Areas with GFP expression were considered as infected when the signal of GFP was significantly higher than 2 S.D. of the mean value of the background signal with Image-Pro Plus® software. The infected area surface was calculated with the same threshold for detection of the GFP signal.

***Statistical procedures*.** Pearson's correlation coefficients were calculated to estimate linear correlations between pairs of variables. We carried out Fisher z-transformations to decrease deviations from normality for parametric t tests. Non parametric Wilcoxon or Mann-Whitney tests were used to assess differences of variables other than correlations. Significance levels were set as $P < 0.05$ and are given for two-tailed tests. To estimate confidence intervals of population vector cross-correlations, cell ensembles were randomly sampled with replacement 500 times to obtain statistical distributions of correlations (bootstrap resampling method).

***Approvals*.** Experiments were performed according to the Norwegian Animal Welfare Act and the European Convention for the Protection of Vertebrate Animals used for Experimental and Other Scientific Purposes. The experiments were approved by the National Animal Research Authorities of Norway.

660 **References**

661 Alme, C.B., Miao, C., Jezek, K., Treves, A., Moser, E.I., and Moser, M.-B. (2014). Place cells in the
662 hippocampus: Eleven maps for eleven rooms. Proceedings of the National Academy of Sciences
663 111(52):18428-35 .

664 Armbruster, B.N., Li, X., Pausch, M.H., Herlitze, S., and Roth, B.L. (2007). Evolving the lock to fit the key
665 to create a family of G protein-coupled receptors potently activated by an inert ligand. Proceedings of
666 the National Academy of Sciences 104, 5163-5168.

667 Battaglia, F.P., and Treves, A. (1998). Attractor neural networks storing multiple space representations:
668 A model for hippocampal place fields. Physical Review E 58, 7738-7753.

669 Boccara, C.N., Sargolini, F., Thoresen, V.H., Solstad, T., Witter, M.P., Moser, E.I., and Moser, M.-B.
670 (2010). Grid cells in pre- and parasubiculum. Nat Neurosci 13, 987-994.

671 Boccara, C. N., Kjonigsen, L. J., Hammer, I. M., Bjaalie, J. G., Leergaard, T. B. and Witter, M. P. (2015) 'A
672 three-plane architectonic atlas of the rat hippocampal region', Hippocampus 25(7): 838-857.

673 Brun, V.H., Leutgeb, S., Wu, H.-Q., Schwarcz, R., Witter, M.P., Moser, E.I., and Moser, M.-B. (2008).
674 Impaired Spatial Representation in CA1 after Lesion of Direct Input from Entorhinal Cortex. Neuron 57,
675 290-302.

676 Chow, B.Y., Han, X., Dobry, A.S., Qian, X., Chuong, A.S., Li, M., Henninger, M.A., Belfort, G.M., Lin, Y.,
677 Monahan, P.E., and Boyden, E.S. (2010). High-performance genetically targetable optical neural
678 silencing by light-driven proton pumps. Nature 463, 98-102.

679 Colgin, L.L., Moser, E.I., and Moser, M.-B. (2008). Understanding memory through hippocampal
680 remapping. Trends in Neurosciences 31, 469-477.

681 de Almeida, L., Idiart, M., and Lisman, J.E. (2012). The single place fields of CA3 cells: A two-stage
682 transformation from grid cells. Hippocampus 22, 200-208.

683 Deller, T., and Frotscher, M. (1997). Lesion-induced plasticity of central neurons: sprouting of single
684 fibres in the rat hippocampus after unilateral entorhinal cortex lesion. Progress in neurobiology 53,
685 687-727.

686 Eichenbaum, H. (2000). A cortical-hippocampal system for declarative memory. Nat Rev Neurosci 1,
687 41-50.

688 Ferbinteanu, J., and Shapiro, M.L. (2003). Prospective and retrospective memory coding in the
689 hippocampus. Neuron 40, 1227-1239.

690 Frank, L.M., Brown, E.N., and Wilson, M. (2000). Trajectory Encoding in the Hippocampus and
691 Entorhinal Cortex. Neuron 27, 169-178.

692 Fuhs, M.C., and Touretzky, D.S. (2006). A Spin Glass Model of Path Integration in Rat Medial Entorhinal
693 Cortex. The Journal of Neuroscience 26, 4266-4276.

694 Fyhn, M., Hafting, T., Treves, A., Moser, M.-B., and Moser, E.I. (2007). Hippocampal remapping and
695 grid realignment in entorhinal cortex. Nature 446, 190-194.

696 Hafting, T., Fyhn, M., Molden, S., Moser, M.-B., and Moser, E.I. (2005). Microstructure of a spatial map
697 in the entorhinal cortex. Nature 436, 801-806.

698 Hales, Jena B., Schlesiger, Magdalene I., Leutgeb, Jill K., Squire, Larry R., Leutgeb, S., and Clark, Robert
699 E. (2014). Medial Entorhinal Cortex Lesions Only Partially Disrupt Hippocampal Place Cells and
700 Hippocampus-Dependent Place Memory. Cell Reports 9, 893-901.

701 Han, X., Chow, B.Y., Zhou, H., Klapoetke, N.C., Chuong, A., Rajimehr, R., Yang, A., Baratta, M.V., Winkle,
702 J., Desimone, R., and Boyden, E.S. (2011). A high-light sensitivity optical neural silencer: development,
703 and application to optogenetic control of nonhuman primate cortex. Frontiers in Systems
704 Neuroscience 5.

705 Hargreaves, E.L., Rao, G., Lee, I., and Knierim, J.J. (2005). Major Dissociation Between Medial and
706 Lateral Entorhinal Input to Dorsal Hippocampus. Science 308, 1792-1794.

707 Hartley, T., Burgess, N., Lever, C., Cacucci, F., and O'Keefe, J. (2000). Modeling place fields in terms of
708 the cortical inputs to the hippocampus. Hippocampus 10, 369-379.

709 Igarashi, K.M., Lu, L., Colgin, L.L., Moser, M.-B., and Moser, E.I. (2014). Coordination of entorhinal-
710 hippocampal ensemble activity during associative learning. Nature *510*, 143-147.
711
712 Ito, H.T., Zhang, S.J., Witter, M.P., Moser, E.I., and Moser, M.B. (2015). A prefrontal-thalamo-
713 hippocampal circuit for goal-directed spatial navigation. Nature 522, 50-55.

714 Jarosiewicz, B., and Skaggs, W.E. (2004). Hippocampal place cells are not controlled by visual input
715 during the small irregular activity state in the rat. J Neurosci 24, 5070-5077.

716 Kentros, C.G., Agnihotri, N.T., Streater, S., Hawkins, R.D., and Kandel, E.R. (2004). Increased attention
717 to spatial context increases both place field stability and spatial memory. Neuron 42, 283-295.

718 Komorowski, R.W., Manns, J.R., and Eichenbaum, H. (2009). Robust conjunctive item-place coding by
719 hippocampal neurons parallels learning what happens where. J. Neurosci. 29, 9918-9929.

720 Langston, R.F., Ainge, J.A., Couey, J.J., Canto, C.B., Bjerknes, T.L., Witter, M.P., Moser, E.I., and Moser,
721 M.-B. (2010). Development of the Spatial Representation System in the Rat. Science 328, 1576-1580.

722 Leutgeb, J. K., Leutgeb, S., Treves, A., Meyer, R., Barnes, C. A., McNaughton, B. L., Moser, M.-B. and
723 Moser, E. I. (2005) 'Progressive Transformation of Hippocampal Neuronal Representations in
724 “Morphed” Environments', Neuron 48(2): 345-358.

725 Leutgeb, S., Leutgeb, J.K., Treves, A., Moser, M.-B., and Moser, E.I. (2004). Distinct Ensemble Codes in
726 Hippocampal Areas CA3 and CA1. Science 305, 1295-1298.

727 Leutgeb, S., Leutgeb, J.K., Barnes, C.A., Moser, E.I., McNaughton, B.L., and Moser, M.-B. (2005).
728 Independent Codes for Spatial and Episodic Memory in Hippocampal Neuronal Ensembles. Science 309,
729 619-623.

730 Leutgeb, S., Leutgeb, J. K., Moser, E. I. and Moser, M.-B. (2006) 'Fast rate coding in hippocampal CA3
731 cell ensembles', Hippocampus 16(9): 765-774.

732 Markus, E.J., Qin, Y.L., Leonard, B., Skaggs, W.E., McNaughton, B.L., and Barnes, C.A. (1995).
733 Interactions between location and task affect the spatial and directional firing of hippocampal neurons.
734 J Neurosci 15, 7079-7094.

735 McNaughton, B.L., Barnes, C.A., and O'Keefe, J. (1983). The contributions of position, direction, and
736 velocity to single unit activity in the hippocampus of freely-moving rats. Exp Brain Res 52, 41-49.

McNaughton, B.L., Battaglia, F.P., Jensen, O., Moser, E.I., and Moser, M.-B. (2006). Path integration and the neural basis of the 'cognitive map'. Nat Rev Neurosci 7, 663-678.

Miller, V.M., and Best, P.J. (1980). Spatial correlates of hippocampal unit activity are altered by lesions of the fornix and endorhinal cortex. Brain Res 194, 311-323.

Monaco, J.D., and Abbott, L.F. (2011). Modular realignment of entorhinal grid cell activity as a basis for hippocampal remapping. The Journal of neuroscience : the official journal of the Society for Neuroscience 31, 9414-9425.

Muller, R.U., and Kubie, J.L. (1987). The effects of changes in the environment on the spatial firing of hippocampal complex-spike cells. J Neurosci 7, 1951-1968.

Muller, R.U., et al. (1991) Spatial firing correlates of neurons in the hippocampal formation of freely moving rats. In Brain and Space (Paillard, J., ed), 296-333, Oxford University Press.

Nadel, L., Samsonovich, A., Ryan, L., and Moscovitch, M. (2000). Multiple trace theory of human memory: computational, neuroimaging, and neuropsychological results. Hippocampus 10, 352-368.

O'Keefe, J. (1976). Place units in the hippocampus of the freely moving rat. Experimental Neurology 51, 78-109.

O'Keefe, J., and Dostrovsky, J. (1971). The hippocampus as a spatial map. Preliminary evidence from unit activity in the freely-moving rat. Brain Research 34, 171-175.

O'Keefe, J., and Nadel, L. (1978). The Hippocampus as a Cognitive Map.

O'Keefe, J., and Speakman, A. (1987). Single unit activity in the rat hippocampus during a spatial memory task. Experimental Brain Research 68, 1-27.

O'Keefe, J., and Burgess, N. (1996). Geometric determinants of the place fields of hippocampal neurons. Nature 381, 425-428.

Ormond, J., and McNaughton, B.L. (2015). Place field expansion after focal MEC inactivations is consistent with loss of Fourier components and path integrator gain reduction. Proceedings of the National Academy of Sciences 112, 4116-4121.

Pavlides, C., and Winson, J. (1989). Influences of hippocampal place cell firing in the awake state on the activity of these cells during subsequent sleep episodes. J Neurosci 9, 2907-2918.

Rolls, E.T., Stringer, S.M., and Elliot, T. (2006). Entorhinal cortex grid cells can map to hippocampal place cells by competitive learning. Network: Computation in Neural Systems 17, 447-465.

Rowland, D.C., and Moser, M.-B. (2014). From cortical modules to memories. Current Opinion in Neurobiology 24, 22-27.

Rueckemann, J. W., DiMauro, A. J., Rangel, L. M., Han, X., Boyden, E. S. and Eichenbaum, H. (2015) Transient optogenetic inactivation of the medial entorhinal cortex biases the active population of hippocampal neurons, Hippocampus, accepted paper.

Sargolini, F., Fyhn, M., Hafting, T., McNaughton, B.L., Witter, M.P., Moser, M.-B., and Moser, E.I. (2006). Conjunctive Representation of Position, Direction, and Velocity in Entorhinal Cortex. Science 312, 758-762.

Savelli, F., and Knierim, J.J. (2010). Hebbian Analysis of the Transformation of Medial Entorhinal Grid-Cell Inputs to Hippocampal Place Fields, Vol 103.

776 Schlesiger, M.I., Cannova, C.C., Boublil, B.L., Hales, J.B., Mankin, E.A., Brandon, M.P., Leutgeb, J.K.,
777 Leibold, C., and Leutgeb, S. (2015). The medial entorhinal cortex is necessary for temporal organization
778 of hippocampal neuronal activity. Nature neuroscience.

779 Scoville, W.B., and Milner, B. (1957). Loss of recent memory after bilateral hippocampal lesions. Journal
780 of Neurology, Neurosurgery, and Psychiatry 20, 11-21.

781 Si, B., and Treves, A. (2009). The role of competitive learning in the generation of DG fields from EC
782 inputs. Cogn Neurodyn 3, 177-187.

783 Solstad, T., Moser, E.I., and Einevoll, G.T. (2006). From grid cells to place cells: A mathematical model.
784 Hippocampus 16, 1026-1031.

785 Solstad, T., Boccara, C.N., Kropff, E., Moser, M.-B., and Moser, E.I. (2008). Representation of Geometric
786 Borders in the Entorhinal Cortex. Science 322, 1865-1868.

787 Squire, L.R. (1992). Memory and the hippocampus: A synthesis from findings with rats, monkeys, and
788 humans. Psychological Review 99, 195-231.

789 Stensola, H., Stensola, T., Solstad, T., Froland, K., Moser, M.-B., and Moser, E.I. (2012). The entorhinal
790 grid map is discretized. Nature 492, 72-78.

791 Van Cauter, T., Poucet, B., and Save, E. (2008). Unstable CA1 place cell representation in rats with
792 entorhinal cortex lesions. European Journal of Neuroscience 27, 1933-1946.

793 Wilson, M., and McNaughton, B. (1994). Reactivation of hippocampal ensemble memories during sleep.
794 Science 265, 676-679.

795 Witter, M.P. (2011). The Hippocampus. In: The Mouse Nervous System. Eds G. Paxinos, L. Puilles & C.
796 Watson. Acad. Press, ch. 5, pp 112-139.

797 Wood, E.R., Dudchenko, P.A., Robitsek, R.J., and Eichenbaum, H. (2000). Hippocampal Neurons Encode
798 Information about Different Types of Memory Episodes Occurring in the Same Location. Neuron 27,
799 623-633.

800 Zhang, S.-J., Ye, J., Miao, C., Tsao, A., Cerniauskas, I., Ledergerber, D., Moser, M.-B., and Moser, E.I.
801 (2013). Optogenetic Dissection of Entorhinal-Hippocampal Functional Connectivity. Science
802 340(6128):1232627.

803

804 **Figure legends**

805 Figure 1. Inhibition of MEC activity with hM4D (A-C) and ArchT (D-F). (A) Spatial map of MEC cells
806 recorded during foraging in a 1 m square box (grid cell, head direction cell and interneuron). Left:
807 colour-coded rate maps; colour scale to the right. Right: trajectory (grey) with spike positions
808 superimposed (black). The cells were from mice with hM4D expression in MEC. (B) Same cells as in (A)
809 recorded before CNO, 30 min after CNO and 12 h after CNO in a 30 cm square box (note scale change
810 from (A)). Spikes are superimposed on the trajectory as in (A). (C) Cumulative frequency diagrams
811 showing percentage change in firing rate 30 min and 12 h after CNO compared to baseline (n = 37).
812 Stippled line indicates no change (100% of baseline level). (D) Spatial map of a different set of MEC

cells in the 1 m square box. The cells were recorded in mice with ArchT expression in MEC. (E) Spike activity of MEC cells in (D) before, during and after laser illumination in the 30 cm square box (5 min each session). (F) Cumulative frequency diagrams showing change in firing rate during and after laser stimulation compared to baseline (n=24). Symbols as in C.

Figure 2. Distribution of MEC infection. (A) Expression of hM4D-GFP in MEC after AAV-hM4D infection across large parts of the MEC (left), in dorsal MEC only (middle), or in ventral MEC only (right). Dorsal and ventral borders of MEC are indicated by white lines. NeuN stains of adjacent sections are shown to indicate distribution of cell bodies in all regions. Scale bar, 1000 µm. (B) Percentage of MEC area with mCitrine expression for mice with widespread AAV-hM4D injections or injections only in dorsal or ventral MEC. (C) Unfolded 'flat' maps of MEC showing the outline of the transfected area in 3 example mice with transfection of both dorsal and ventral MEC (large) or only dorsal or ventral MEC.

Figure 3. Partial inactivation of MEC did not change the firing properties of place cells. (A) Left panel: Sagittal brain section showing expression of hM4D-mCitrine(Green) across a substantial part of the dorsoventral MEC axis. Dorsal and ventral borders of MEC are indicated by white lines. Expression is also seen in axonal projections into the hippocampus to the left of the MEC. Scale bar, 800 µm. Right panel: Nissl-stained sagittal brain section showing position of tetrode (arrow) in the same animal. (B) Colour-coded rate maps showing firing locations of a representative CA3 place cell on the linear track before CNO, 30 min after CNO, and 12 h after CNO. Colour scale to the right. (C and D) Cumulative frequency diagrams showing no change in mean firing rate or spatial information of place fields after CNO in hM4D-expressing animals. (E-G) Population vector cross-correlation matrices for the baseline trial (E), 30 min after CNO (F), and 12 h after CNO (G). Analyses include all place cells from all animals in the experimental group. (H) Overlaid decorrelation curves showing mean correlation (solid lines) ± 95% confidence intervals (shaded color) for each possible population vector pair distance between 0 and 10 bins (4 cm each bin). The confidence intervals were estimated by a bootstrap resampling procedure. To quantify the scale of the spatial representation, the distance at which the correlation dropped to r = 0.2 was calculated. Note similar distances before, during and after CNO.

Figure 4. Partial inactivation of MEC induced remapping in CA3 place cells. (A) Colour-coded population map showing location of CA3 place fields before CNO, 30 min after CNO, and 12 h after CNO. Each line shows activity of one place cell in one running direction (109 data sets in total from 75 place cells).

Colour indicates firing rate (scale bar to the right). Firing rate was normalized for each cell to the cell's baseline firing rate. Cells are sorted according to position of the place field (centre of mass) during the baseline trial. The sequence of cells is the same for all three plots (before CNO, 30 min after and 12 h after). (B) Cumulative frequency distributions showing spatial correlations and population vector correlations for different pairs of epochs in the CNO experiment: first vs. second half of the baseline period, 30 min post-CNO vs. baseline, and 12 h post-CNO vs. baseline. Data are shown for all animals with hM4D expression in dorsal, ventral or dorsal-and-ventral MEC (top) as well as control animals with GFP expression only (bottom). Spatial correlation for shuffled pairs of distributions is shown for comparison.

Figure 5. Comparion of dorsal and ventral MEC inactivation. (A and F) Sagittal brain sections showing expression of hM4D-mCitrine(Green) in dorsal and ventral MEC, respectively (left panel) and the same sections stained for NeuN (right panel). Scale bar, 800 μm. (B and G) Colour-coded rate maps showing firing locations of representative CA3 place cells on the linear track before CNO, 30 min after CNO, and 12 h after CNO. Colour scales to the right. (C and H) Colour-coded population maps showing changes in firing locations of CA3 place fields after CNO. Dorsal MEC group (C): n = 30, ventral MEC group (H): n = 28. Symbols as in Figure 4A. (D and H) Cumulative frequency distributions showing population vector correlations between different epochs of the CNO experiment. Symbols as in Figure 4B. (E and J) Population vector cross-correlation matrices from baseline, 30 min after CNO, and 12 h after CNO. Decorrelation curves in the bottom right quadrants show similar mean distances for all possible population vector pairs at values up to 10 bins (4cm each bin). Symbols as in Figure 3E-H.

Figure 6. Lap-by-lap analysis of population vectors. The analysis includes a total of 30 laps (10 from the baseline, 10 from the MEC inactivation, and 10 from the recovery session). Population vectors were defined for each spatial bin of the linear track. Population vectors on individual laps were then correlated with the average of the last 10 laps of the baseline session (blue), the average of the first 10 laps of the MEC inactivation (red), or the average of the first 10 laps of the recovery session (green). Plots show mean population vector correlations across 20 spatial bins (solid lines) with SEM (shaded colors). (A) Lap-by-lap population vector correlations before and after CNO in mice injected with AAV-hM4D in MEC. (B) Similar correlations in control mice injected with AAV-GFP in MEC. (C) Lap-by-lap population vector correlations before and after light stimulation in mice injected with AAV-ArchT in MEC. (D) Laser stimulation in control mice injected with AAV-GFP. Note abrupt change in population

877 vector correlations at the onset of MEC silencing. The change was not observed in control mice
878 injected with CNO or laser illumination.

879

880 Figure 7. Inactivation of axons from MEC induced remapping in CA3 place cells. (A) Left panel: Sagittal
881 brain section showing expression of ArchT-GFP(Green) protein in MEC. Dorsal and ventral borders of
882 MEC are indicated by white lines. Scale bar, 800 μm. Right panel: NIssl-stained sagittal brain section
883 showing position of tetrode (arrow) and optical fiber in the hippocampus; symbols as in Figure 2A. (B)
884 Example of CA3 place cells before, with and after laser illumination. (C) Cumulative frequency diagrams
885 showing decreased mean firing rate and spatial information in place cells of ArchT-expressing animals
886 during and after laser stimulation. (D) Colour-coded population map showing firing locations of CA3
887 place cells before, with and after laser illumination (n = 83). Symbols as in Figure 4A. (E) Distribution
888 of spatial correlations and population vector correlations for pairs of sessions in the laser experiment,
889 as in Figure 4B.

890

891 Figure S1. Unfolded 'flat' maps showing extent and position of AAV-infected areas for all animals. Page
892 1 & 2: Flat maps for MEC. Page 3: postrhinal cortex. Page 4: parasubiculum. Page 5: presubiculum. Page
893 6: lateral entorhinal cortex (LEC). Page 7: subiculum. Flat maps were generated by mapping for each
894 structure the dorsoventral extent of the area in each brain section as well as the infected area along
895 the same extent. We used stable borders as the reference for alignment, with this reference presented
896 on the vertical axis. Individual sections and infected areas are shown as rows. For MEC, the dorsal
897 border, either with the postrhinal cortex or the parasubiculum, was used as reference. For the
898 postrhinal cortex we used its ventral border, either with MEC or parasubiculum. For pre- and
899 parasubiculum, the borders with subiculum and MEC, respectively, were used as references. For LEC,
900 sections were aligned to the border with MEC, and for subiculum we used the border with CA1 as the
901 reference. In all flat maps, green areas represent mCitrine-expressing and GFP-expressing (AAV-hM4D
902 or AAV-ArchT infected) regions. It can be seen that infections were largely restricted to MEC (see also
903 Supplemental Table 1). In hM4D-expressing animals, 18.7% of the infected area was outside MEC
904 (lateral entorhinal cortex, pre- and parasubiculum, or postrhinal cortex). In ArchT-expressing animals,
905 19.2% was outside MEC.

906

907 Figure S2. mCitrine and GFP expression in MEC. Top row (A-D), hM4D-infected animal. Bottom row
908 (E-H), ArchT-infected animal. (A and E): low-magnification images with white boxes showing location

of high-magnification images in B-D and F-H, respectively. Note that the majority of MEC cells express hM4D or ArchT in the infected region. Expression of mCitrine or GFP is shown in green and NeuN in red. Scale bars in A and E are 200 μm. Bars in B to D and F to H are 50 μm.

Figure S3. mCitrine and GFP are not expressed in hippocampal cells after injection of AAV. (A-C) hM4D-mCitrine-expressing cells in green; NeuN and DAPI in red and blue, respectively. B and C are high magnification images taken at the location indicated by the white boxes indicated in A (B left box, C right box). None of the mice in the hM4D group showed retrograde mCitrine labeling (green) in hippocampal neurons, labeled by NeuN, or in any hippocampal cell, labeled by DAPI, after injection of AAV-hM4D in the MEC. Label was only observed in axons. Scale bar in A is 200 μm. Bars in B and C are 50 μm. (D-F) ArchT-GFP-expressing cells in green; NeuN and DAPI in red and blue, respectively. E and F are high magnification images taken from the white boxes in D (E left box, F right box). Scale bar in D is 200 μm. Bars in E and F are 50 μm. In 6 out of 8 ArchT-infected mice, there were no retrogradely labeled hippocampal neurons after injection of AAV-ArchT in MEC. In the remaining two mice, retrograde expression was observed only in the pyramidal cell layer of CA2 (shown in Figure S4). Medial entorhinal axons were labeled in subiculum (not shown), CA1, CA3 and DG. (G-I) TUNEL staining shows absence of apoptotic neurons in the hippocampus after laser illumination (3 to 5 min continuous illumination). (G) TUNEL stain of a section through the hippocampus; scale bar is 200 μm; (H) Positive control using cell suspension provided by Abcam (see methods). Pink signal shows apoptotic cells; (I) Negative cell-suspension control. Bars in H and I are 50 μm.

Figure S4. Retrograde infection outside MEC after injection of AAV-ArchT in MEC of 2 mice. (A-D) Expression of ArchT-GFP in MEC and adjacent structures. ArchT-GFP is shown in green (A), NeuN is shown in red (B), DAPI is shown in blue (C). D. Merged image of A-C., showing additional sparse labeling in the granule cell layer of DG (arrow), pre- and parasubiculum (open arrows), subiculum (arrowhead), and postrhinal cortex (asterisk). Marked retrograde labeling can also be seen in CA2 (boxed area in A, magnified in E – H). Scale bars, 200 μm. (E - H) Retrograde labeling with ArchT-GFP of neurons in CA2. Scale bars, 100 μm. (E-H) are high power images from the box in A.

Figure S5. (A) c-Fos expression 30 min after injection of CNO in AAV-hM4D-injected MEC on ipsilateral and contralateral side. Expression of GFP is shown in green, NeuN and c-fos in red, and DAPI in blue.

940 Scale bar in (A), 100 µm. (B) Number of c-fos positive cells in virus-expressing and contralateral
941 hemispheres. *, $P < 0.05$.

942

943 Figure S6. Simultaneous recording in MEC and dorsal-intermediate hippocampus during inactivation in
944 the dorsal MEC of mice injected with AAV-hM4D. (A) Rate map of spatial cells from MEC and place cells
945 from CA3 before, 30 min and 12 h after injection of CNO. (B) Colour-coded neural population map
946 showing location of CA3 place fields and MEC spatial cells before CNO, 30 min after CNO, and 12 h
947 after CNO. Each line corresponds to one field (n = 14). (C) Cumulative frequency distribution showing
948 spatial correlations (C) and population vector correlations (D) for epochs of the CNO experiment, as in
949 Figure 4B.

950

951 Figure S7. Cumulative frequency diagrams showing remapping following light stimulation in place cells
952 in Arch-T expressing mice without retrograde infection in CA2. Symbols as in Figure 3C. Left panel:
953 Spatial correlation. Right panel: Population vector correlation.

954

955 Supplemental figure 1 for Reviewers. Power spectral of local field potential after inhibition of MEC. (A)
956 Gamma power before and after MEC inhibition was analyzed for different running speeds: 5cm/s,
957 10cm/s, 15cm/s and 20cm/s. We distinguished between fast gamma range (60Hz to 90Hz) and slow
958 gamma range (25Hz to 45Hz). (A) In the hM4D group, fast gamma power was not significant changed
959 after CNO (before CNO, fast gamma power: 11.9 ± 1.8; 30 min after CNO, fast gamma power: 11.4 ±
960 1.8, Wilcoxon signed rank test, $Z = 1.795$, $P = 0.073$). Slow gamma power was slightly decreased (before
961 CNO, slow gamma power: 18.2 ± 1.9; 30 min after CNO, slow gamma power: 17.2 ± 1.9, Wilcoxon
962 signed rank test, $Z = 4.21$, $P = 2.56 \times 10^{-5}$). (B)In the ArchT group, fast gamma power was slightly
963 decreased during laser stimulation (before laser, fast gamma power: 18.2 ± 1.9; with laser, fast gamma
964 power: 17.2 ± 1.9, Wilcoxon signed rank test, $Z = 2.39$, $P = 0.017$). Slow gamma power was slightly
965 decreased (before laser, slow gamma power: 14.3 ± 1.88; with laser, slow gamma power: 13.4 ± 1.9,
966 Wilcoxon signed rank test, $Z = 4.89$, $P = 1.14 \times 10^{-6}$).

967

968 Supplemental figure 2 for Reviewers. Phase precession of place fields after inhibition of MEC. We
969 examined the number of the place fields that exhibited significant phase precession, using the same
970 methods for calculation of phase precession as in previous work (Hafting et al., 2008, Nature). (A) In

971 the hM4D group, 25 out 104 place fields (24%) exhibited clear phase precession before CNO. The
972 number decreased nonsignificantly to 18 out of 90 place fields (20%) 30 min after CNO ($Z = 0.675$, $P =$
973 0.499, binomial test). For place fields with significant phase precession, the mean slope of precession
974 did not exhibit significant change 30 min after CNO (before CNO: -8.85 ± 2.32 degree/cm; 30min after
975 CNO: -8.22 ± 1.13 degree/cm). (B) In the ArchT group, 30 out 79 place fields (38%) exhibited clear phase
976 precession before laser stimulation. The number decreased to 9 out of 59 place fields during
977 stimulation (15%) ($Z = 2.93$, $P = 0.003 < 0.01$ binomial test). The proportion of cells with clear phase
978 precession increased after the laser trial (16 out 66 place fields [24%], $Z=1.77$, $P = 0.08$). For place fields
979 with significant phase precession, the mean slope of precession did not change significantly with laser
980 illumination (before laser: -18.1 ± 8.76 degree/cm; with laser -4.6 ± 0.84 degree/cm, $D = 0.33$ $P = 0.35$).

Figures 1-7

Figure 1

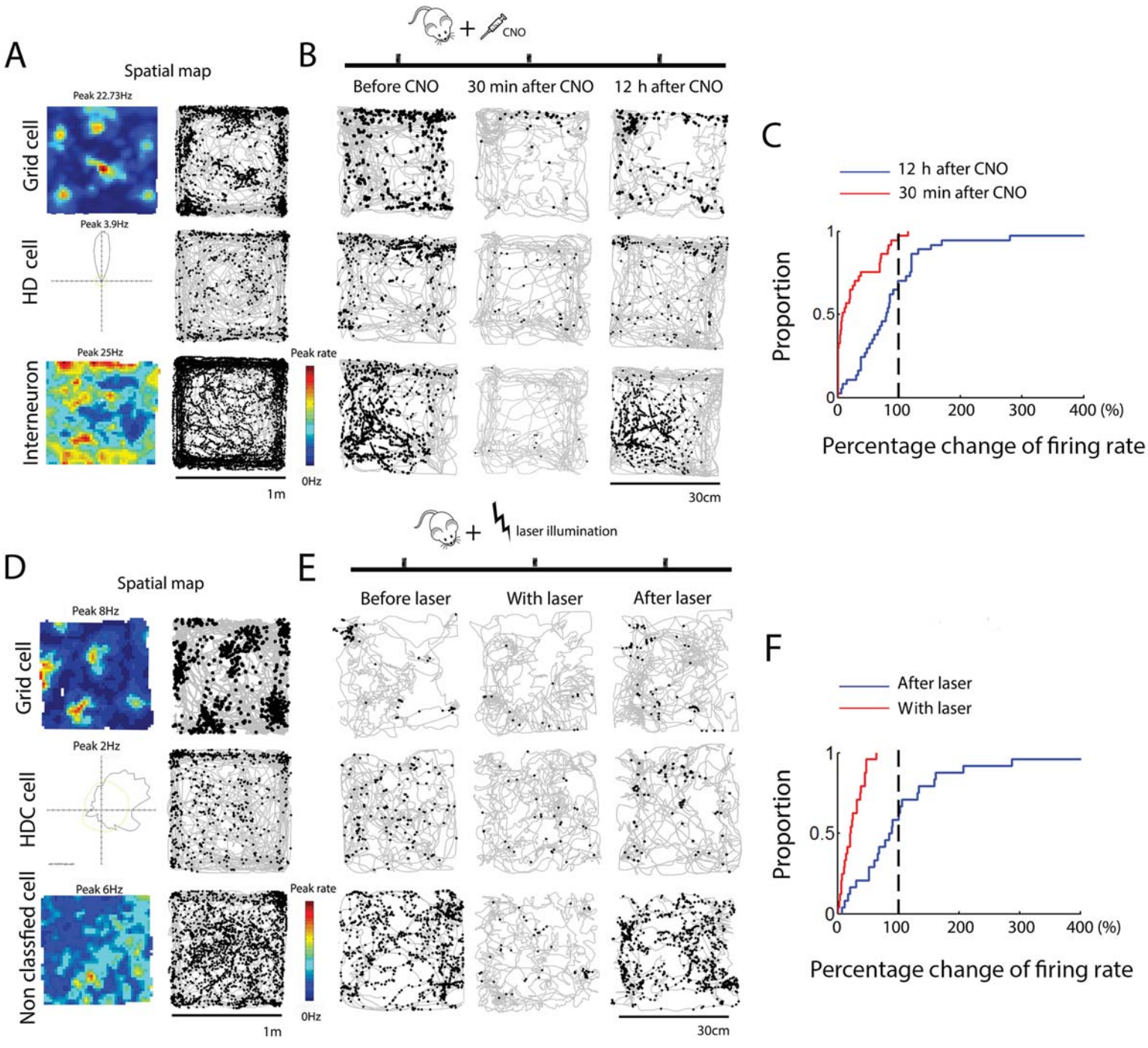

Figure 2

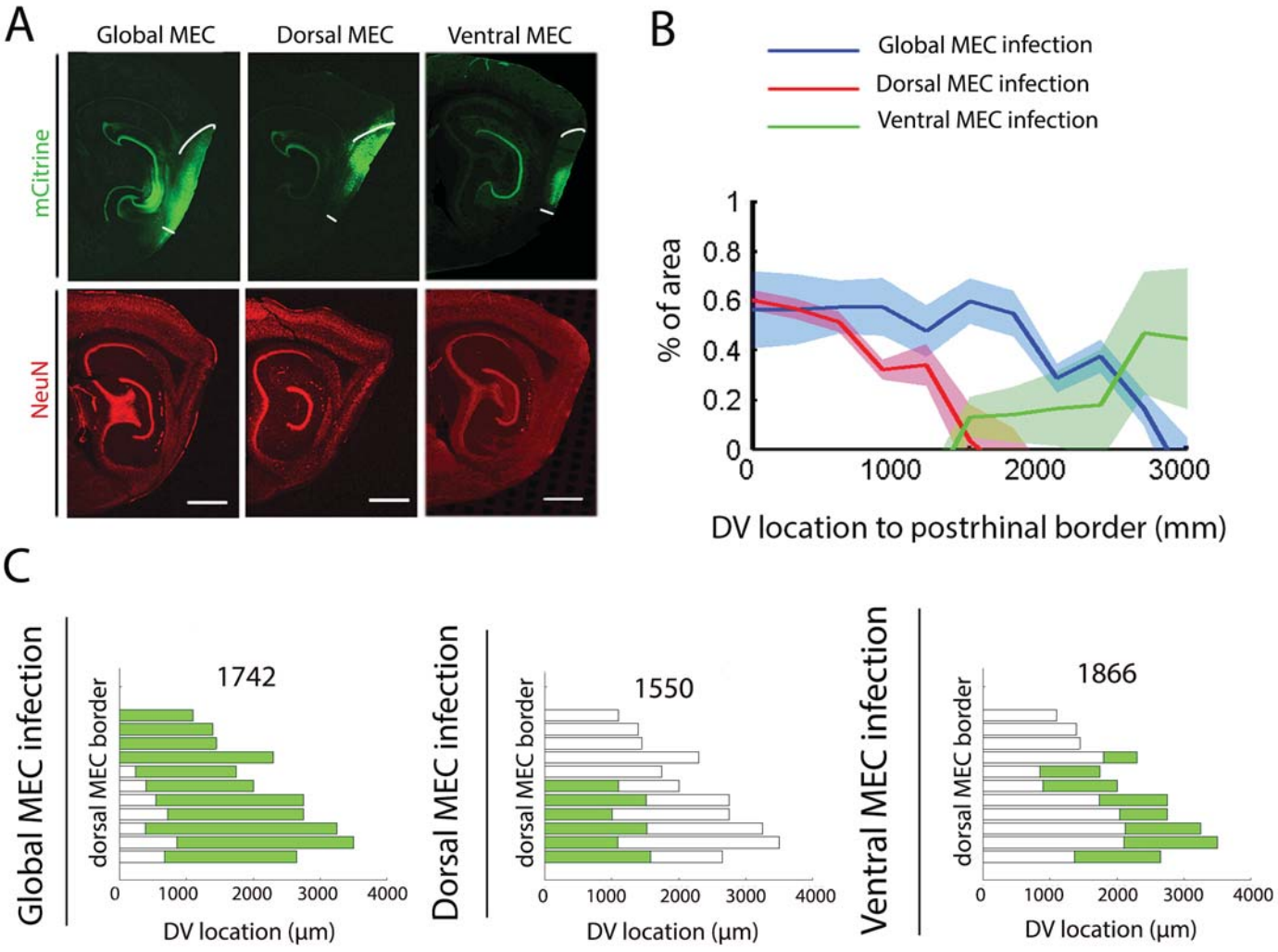
A
Global MEC
Dorsal MEC
Ventral MEC
mCitrine
NeuN
B
Global MEC infection
Dorsal MEC infection
Ventral MEC infection
% of area
1
0.8
0.6
0.4
0.2
0
0
1000
2000
3000
DV location to postrhinal border (mm)
C
Global MEC infection
dorsal MEC border
1742
0
1000
2000
3000
4000
DV location (μm)
Dorsal MEC infection
dorsal MEC border
1550
0
1000
2000
3000
4000
DV location (μm)
Ventral MEC infection
dorsal MEC border
1866
0
1000
2000
3000
4000
DV location (μm)

Figure 3

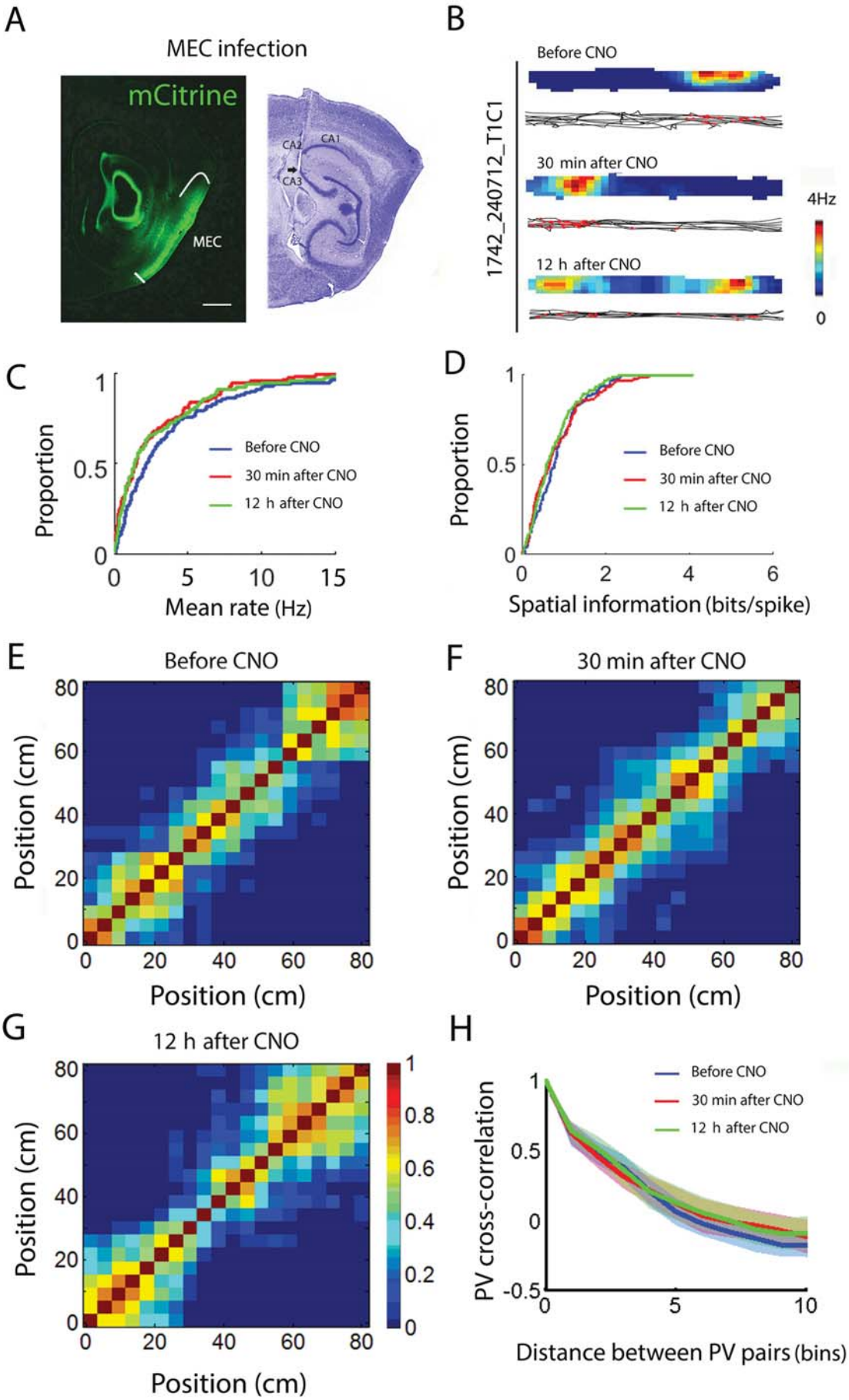
A
MEC infection
mCitrine
MEC
CA2
CA1
CA3
B
Before CNO
30 min after CNO
12 h after CNO
1742_240712_T1C1
4Hz
0
C
Proportion
Mean rate (Hz)
Before CNO
30 min after CNO
12 h after CNO
D
Proportion
Spatial information (bits/spike)
Before CNO
30 min after CNO
12 h after CNO
E
Before CNO
Position (cm)
Position (cm)
F
30 min after CNO
Position (cm)
Position (cm)
G
12 h after CNO
Position (cm)
Position (cm)
H
PV cross-correlation
Distance between PV pairs (bins)
Before CNO
30 min after CNO
12 h after CNO

Figure 4

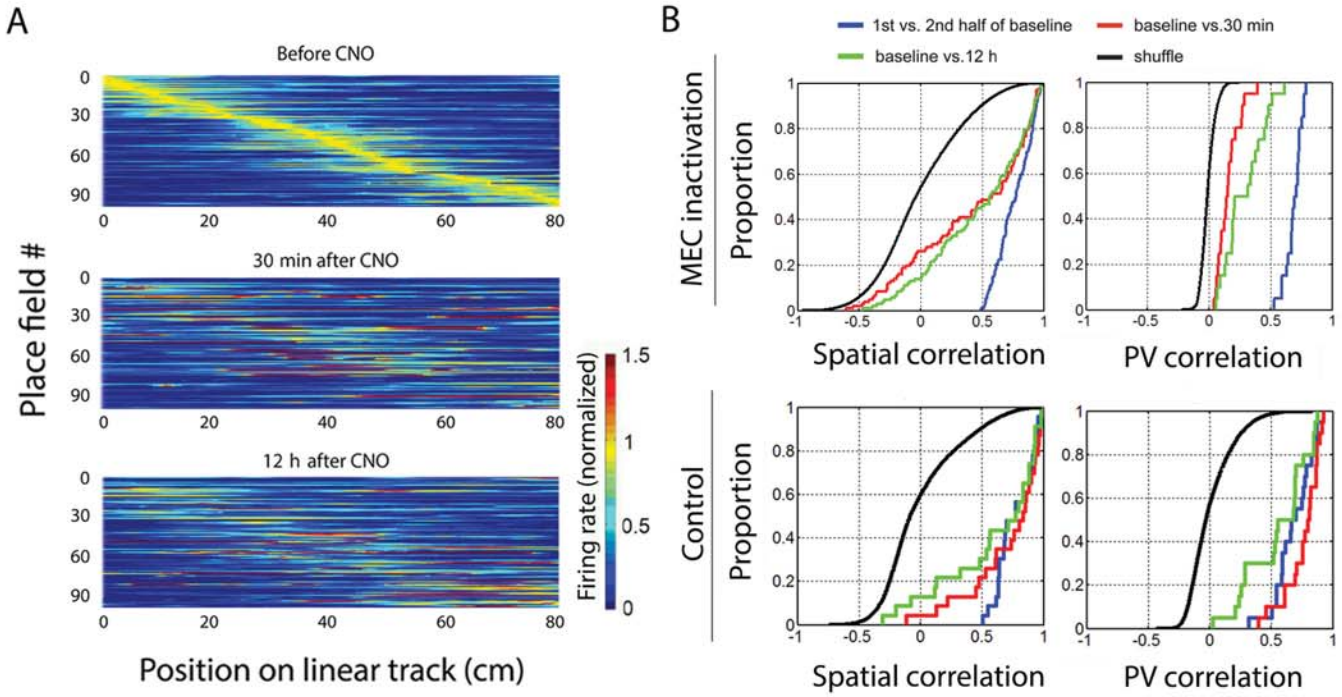
A
Before CNO
30 min after CNO
12 h after CNO
Place field #
Position on linear track (cm)
Firing rate (normalized)
B
1st vs. 2nd half of baseline
baseline vs.30 min
baseline vs.12 h
shuffle
MEC inactivation
Control
Proportion
Spatial correlation
PV correlation

Figure 5

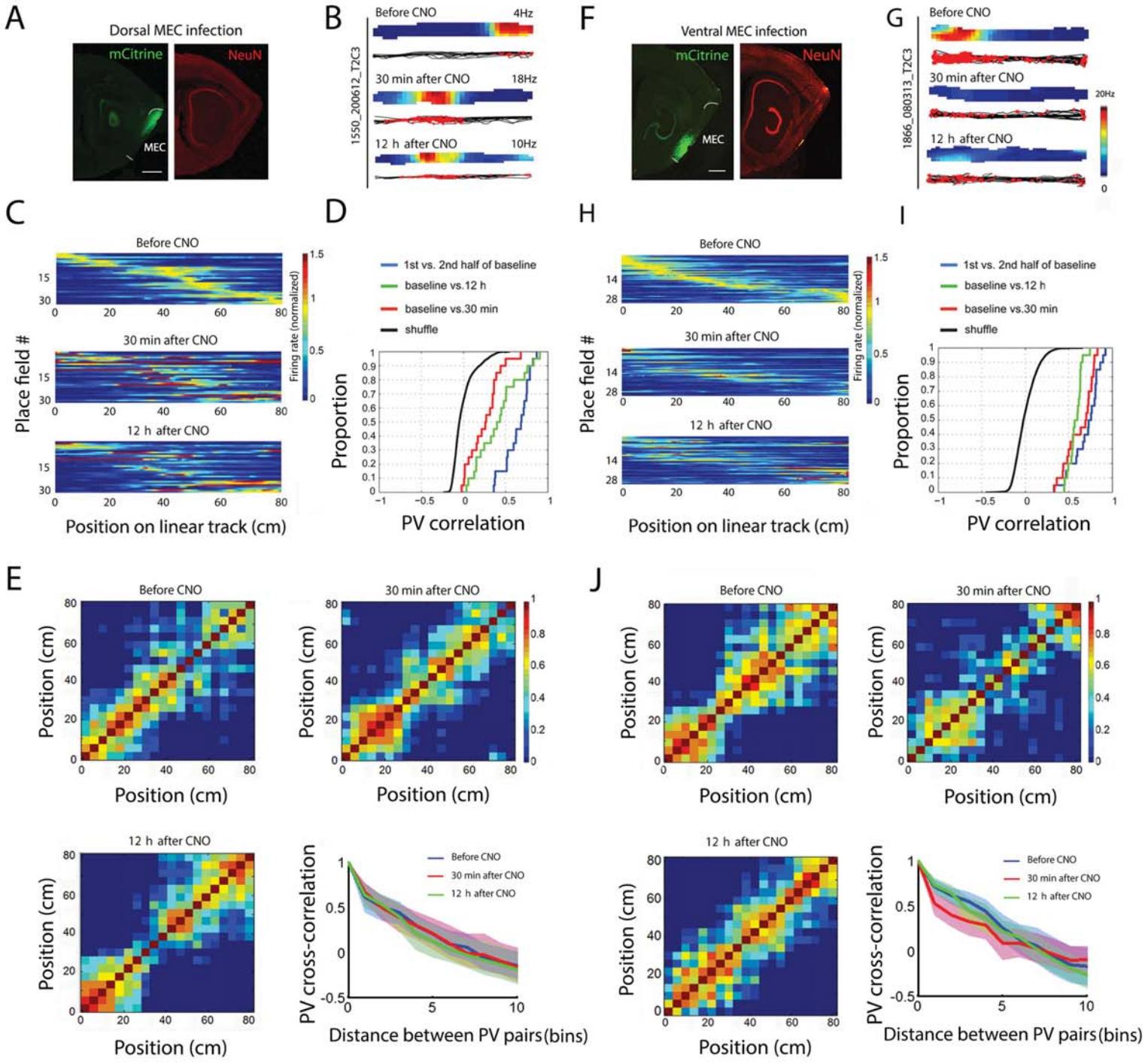
A
Dorsal MEC infection
mCitrine
NeuN
MEC
B
Before CNO
4Hz
1550_200612_T2C3
30 min after CNO
18Hz
12 h after CNO
10Hz
F
Ventral MEC infection
mCitrine
NeuN
MEC
G
Before CNO
1866_080313_T2C3
30 min after CNO
20Hz
12 h after CNO
0
C
Before CNO
30 min after CNO
12 h after CNO
Place field #
Firing rate (normalized)
Position on linear track (cm)
D
1st vs. 2nd half of baseline
baseline vs.12 h
baseline vs.30 min
shuffle
Proportion
PV correlation
H
Before CNO
30 min after CNO
12 h after CNO
Place field #
Firing rate (normalized)
Position on linear track (cm)
I
1st vs. 2nd half of baseline
baseline vs.12 h
baseline vs.30 min
shuffle
Proportion
PV correlation
E
Before CNO
30 min after CNO
12 h after CNO
Position (cm)
PV cross-correlation
Before CNO
30 min after CNO
12 h after CNO
Distance between PV pairs (bins)
J
Before CNO
30 min after CNO
12 h after CNO
Position (cm)
PV cross-correlation
Before CNO
30 min after CNO
12 h after CNO
Distance between PV pairs (bins)

Figure 6

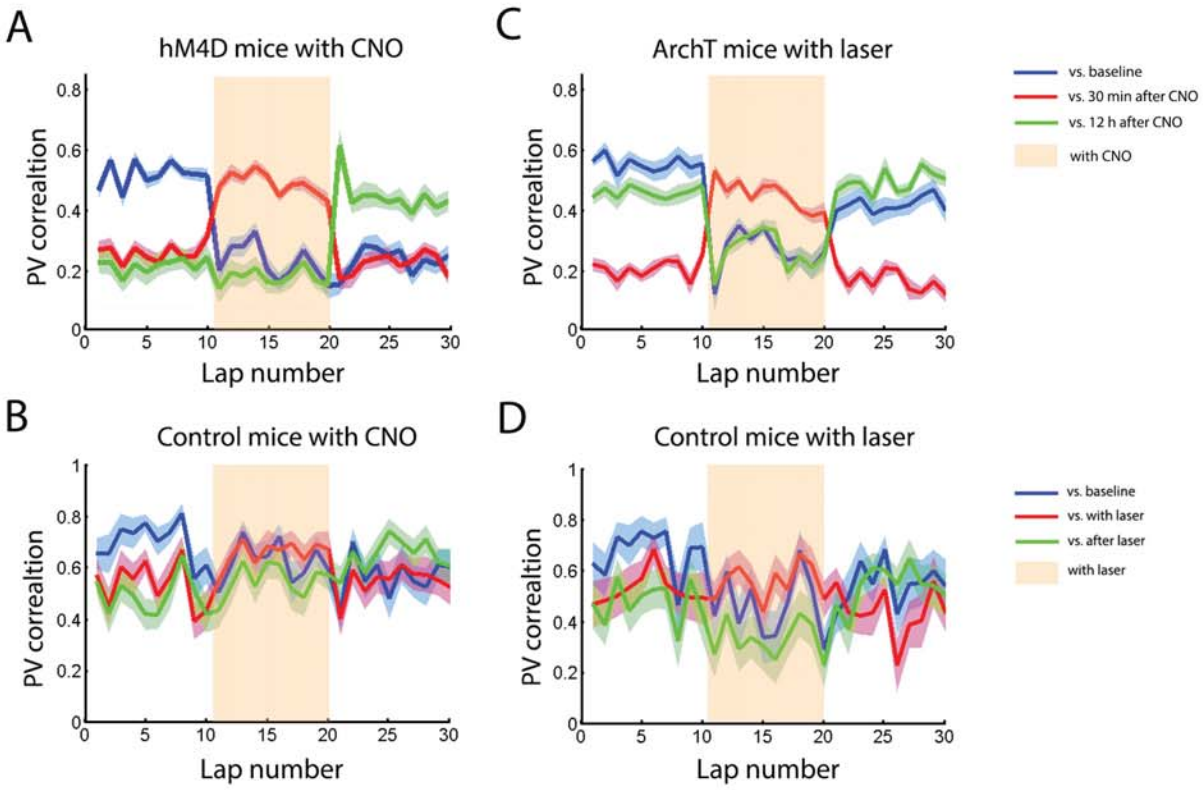
A
hM4D mice with CNO
PV correaltion
Lap number
C
ArchT mice with laser
PV correaltion
Lap number
vs. baseline
vs. 30 min after CNO
vs. 12 h after CNO
with CNO
B
Control mice with CNO
PV correaltion
Lap number
D
Control mice with laser
PV correaltion
Lap number
vs. baseline
vs. with laser
vs. after laser
with laser

Figure 7

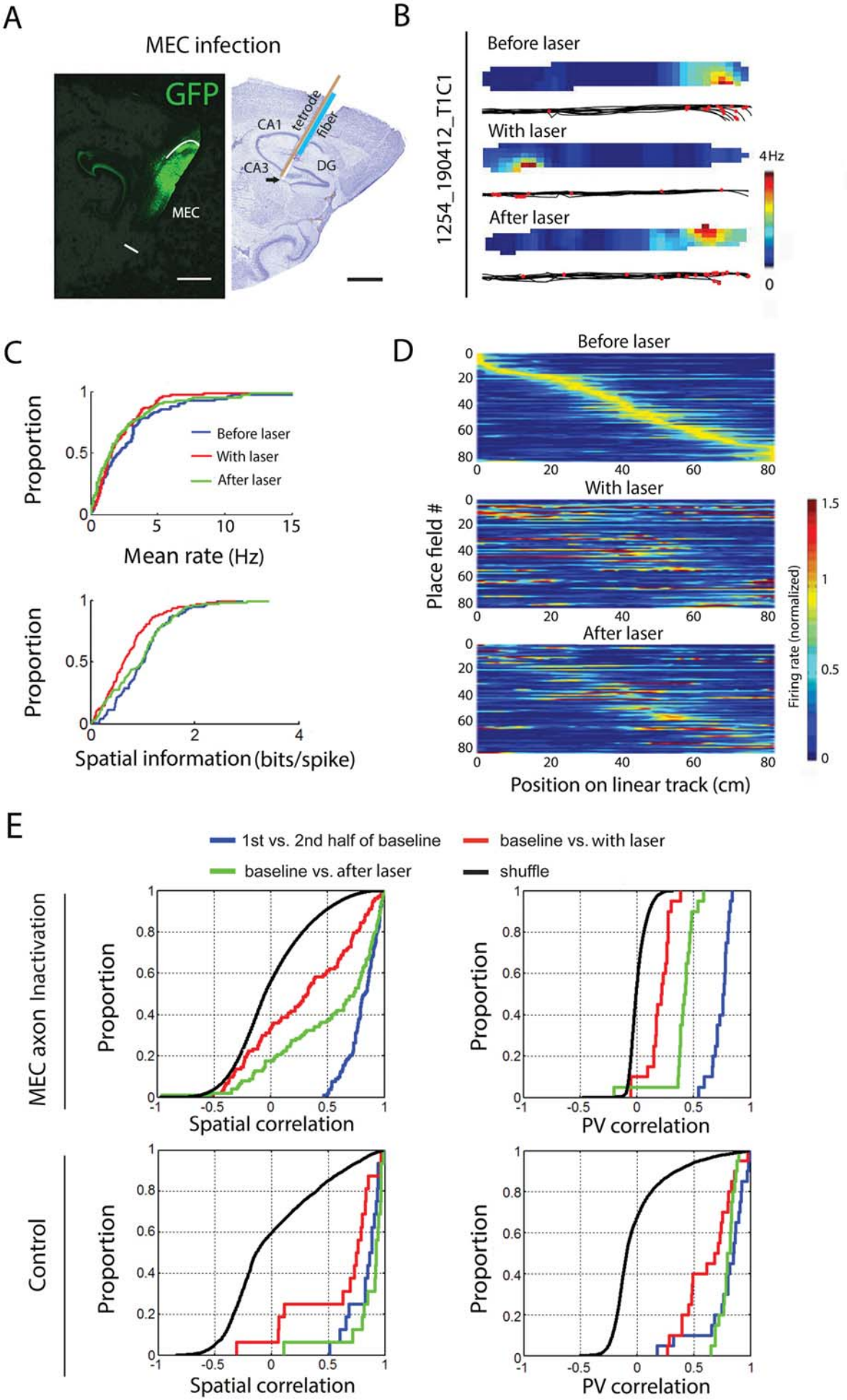
A
MEC infection
GFP
MEC
CA1
CA3
DG
tetrode
fiber
B
1254_190412_T1C1
Before laser
With laser
After laser
4Hz
0
C
Proportion
Before laser
With laser
After laser
Mean rate (Hz)
Spatial information (bits/spike)
D
Before laser
With laser
After laser
Place field #
Firing rate (normalized)
Position on linear track (cm)
E
1st vs. 2nd half of baseline
baseline vs. with laser
baseline vs. after laser
shuffle
MEC axon Inactivation
Control
Proportion
Spatial correlation
PV correlation

Supplemental figure 1

Flat maps for MEC

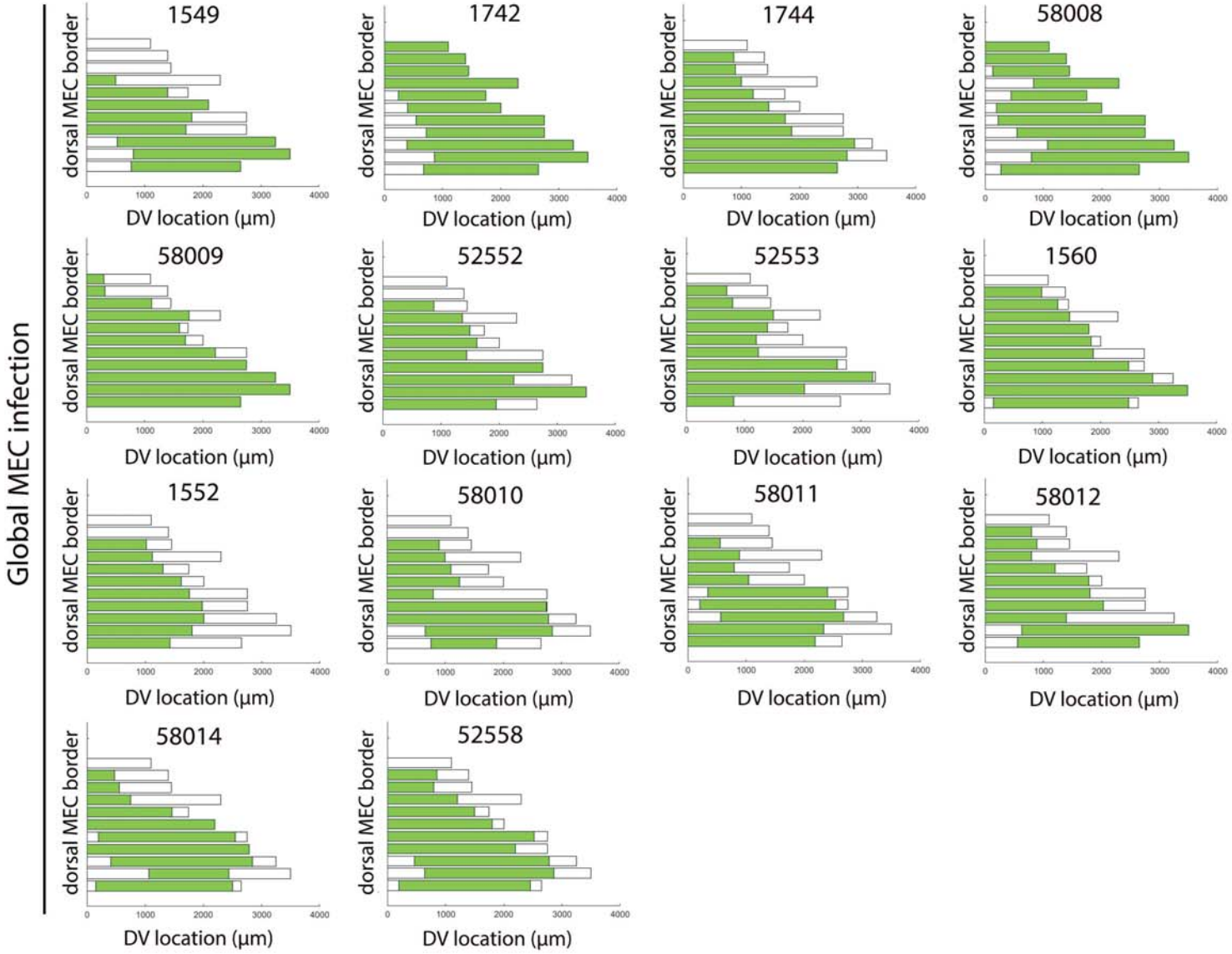

Supplemental figure 1

Flat maps for MEC

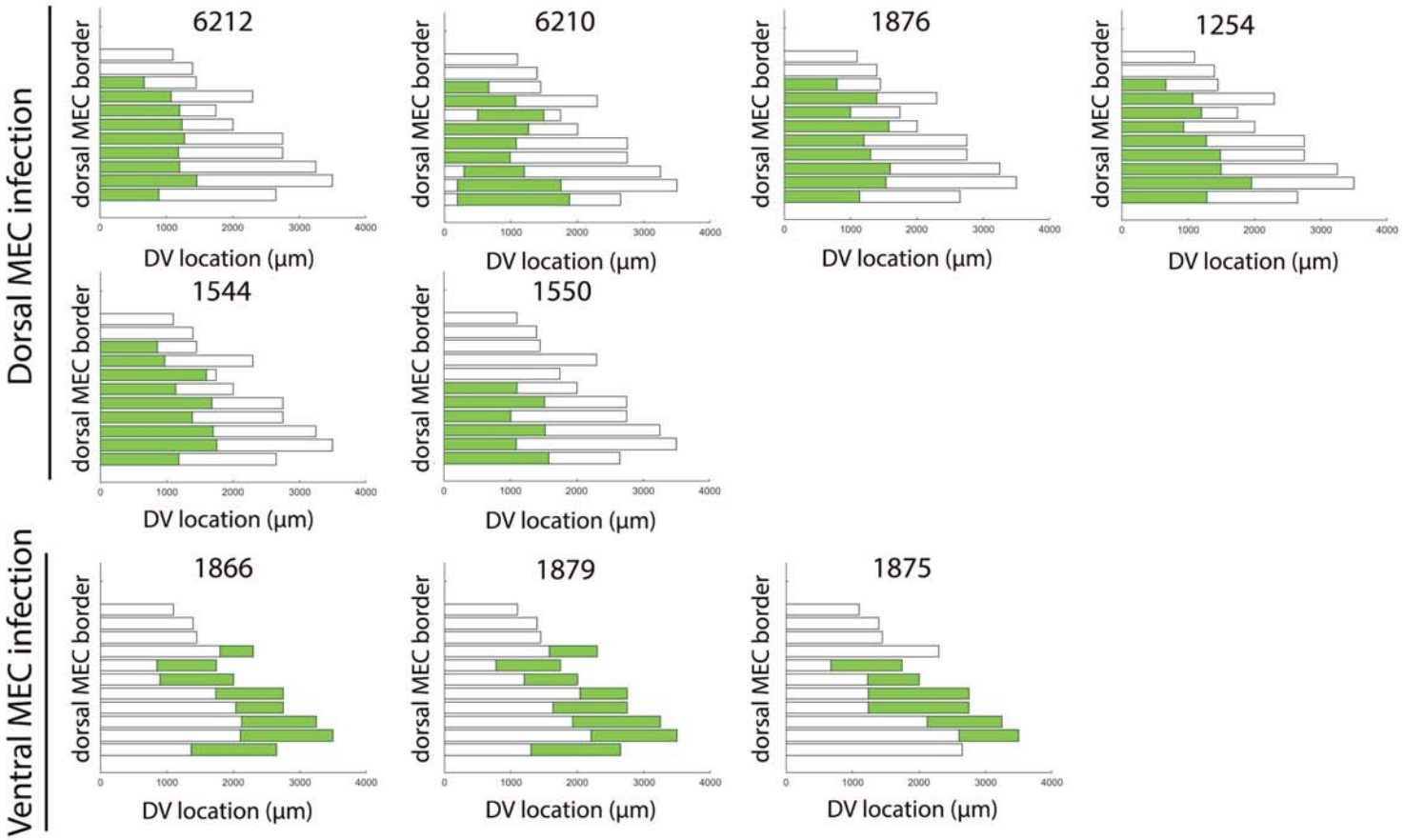

Supplemental figure 1

Flat maps for postrhinal cortex

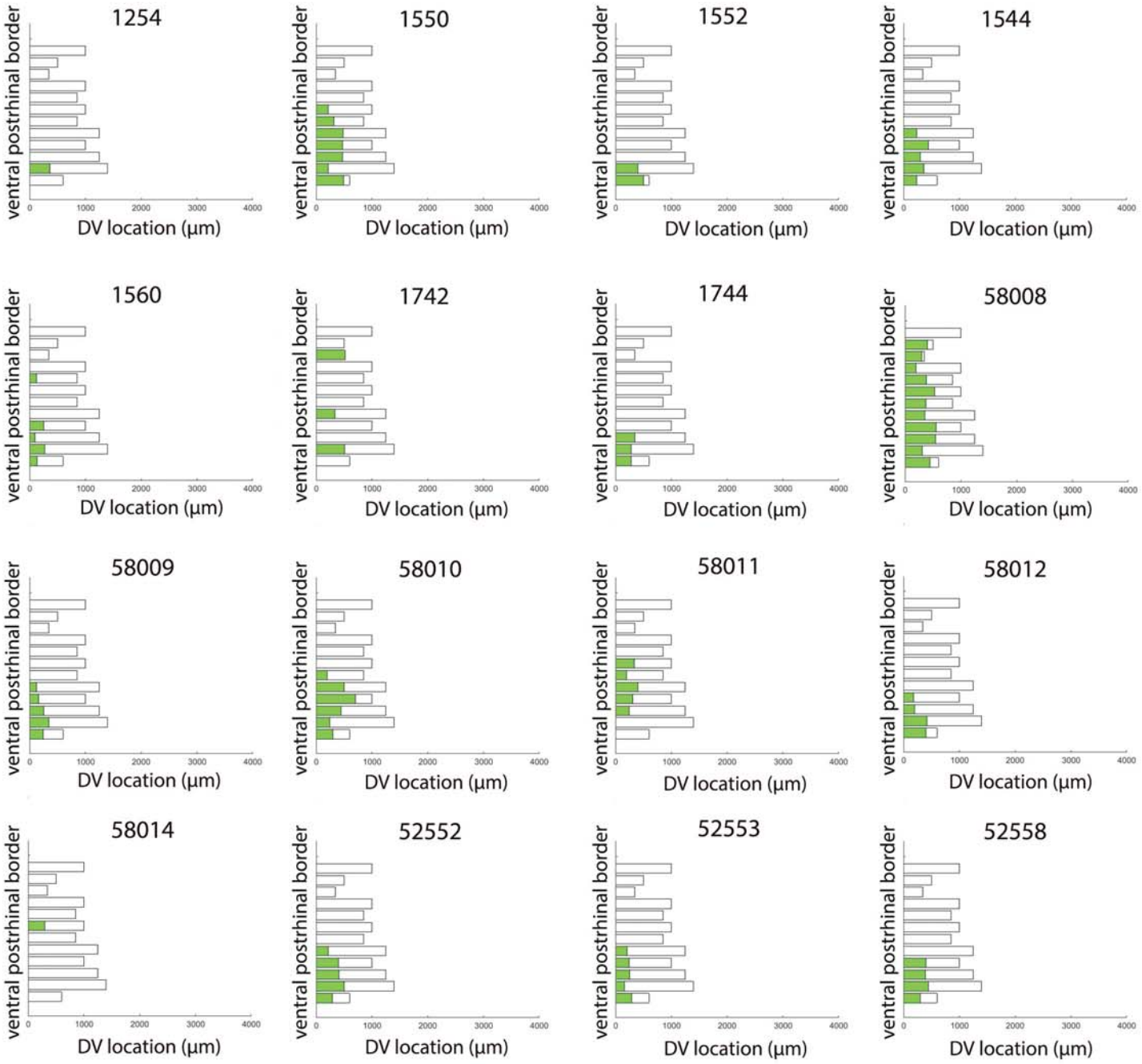

Supplemental figure 1

Flat maps for parasubiculum

Supplemental figure 1

Flat maps for presubiculum

Supplemental figure 1

Flat maps for lateral entorhinal cortex

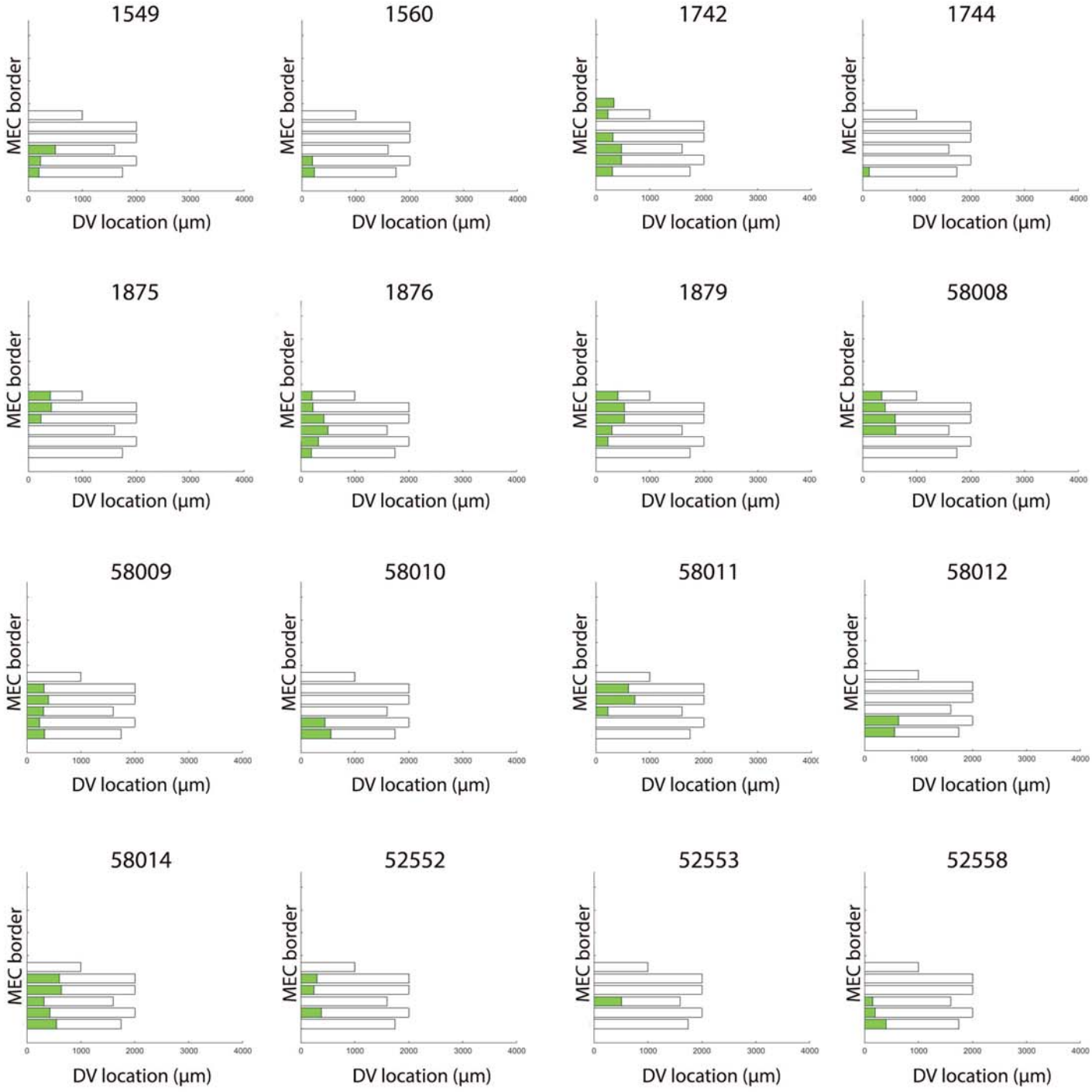

Supplemental figure 1

Flat maps for subiculum

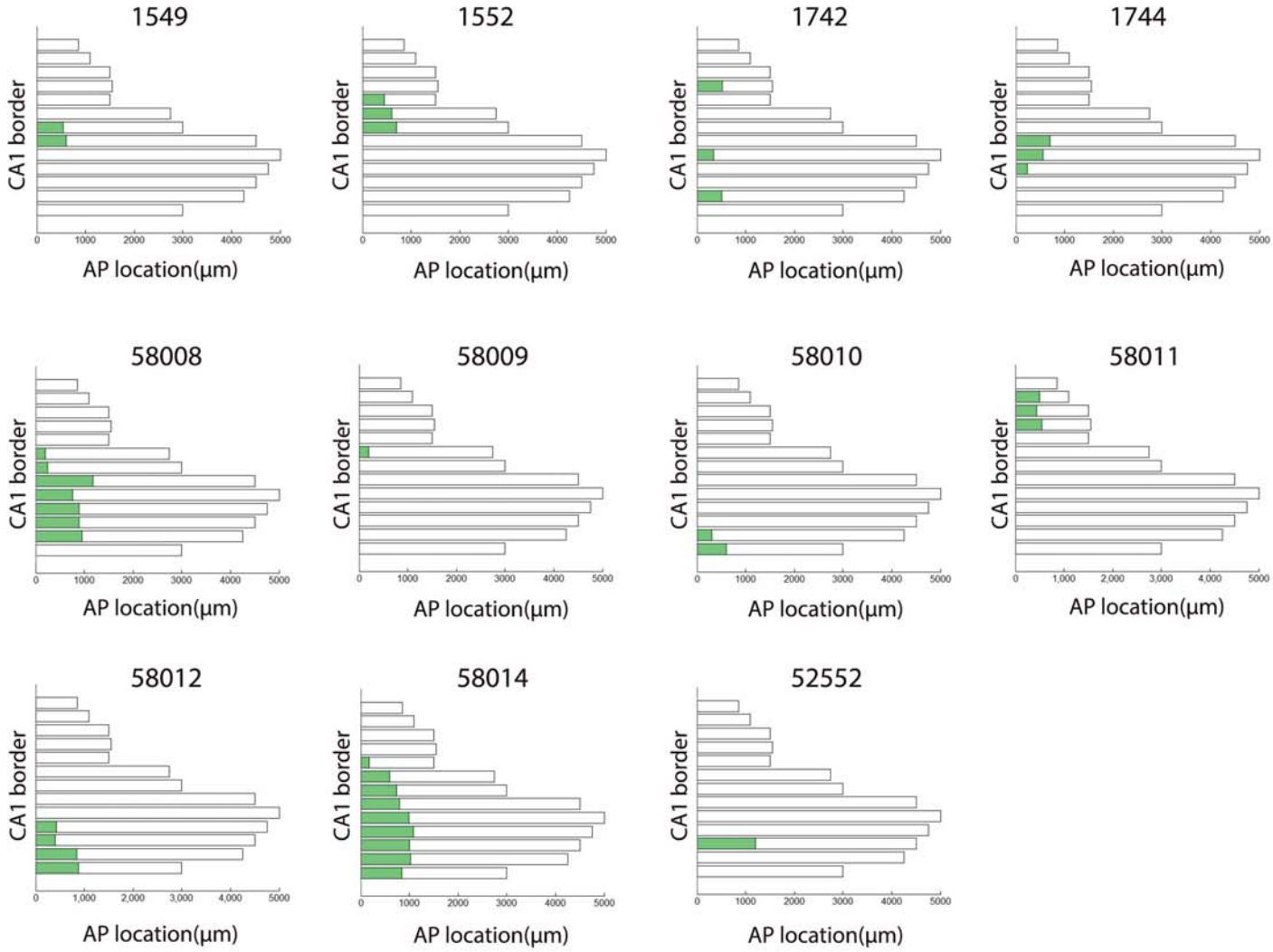

Supplemental figure 2

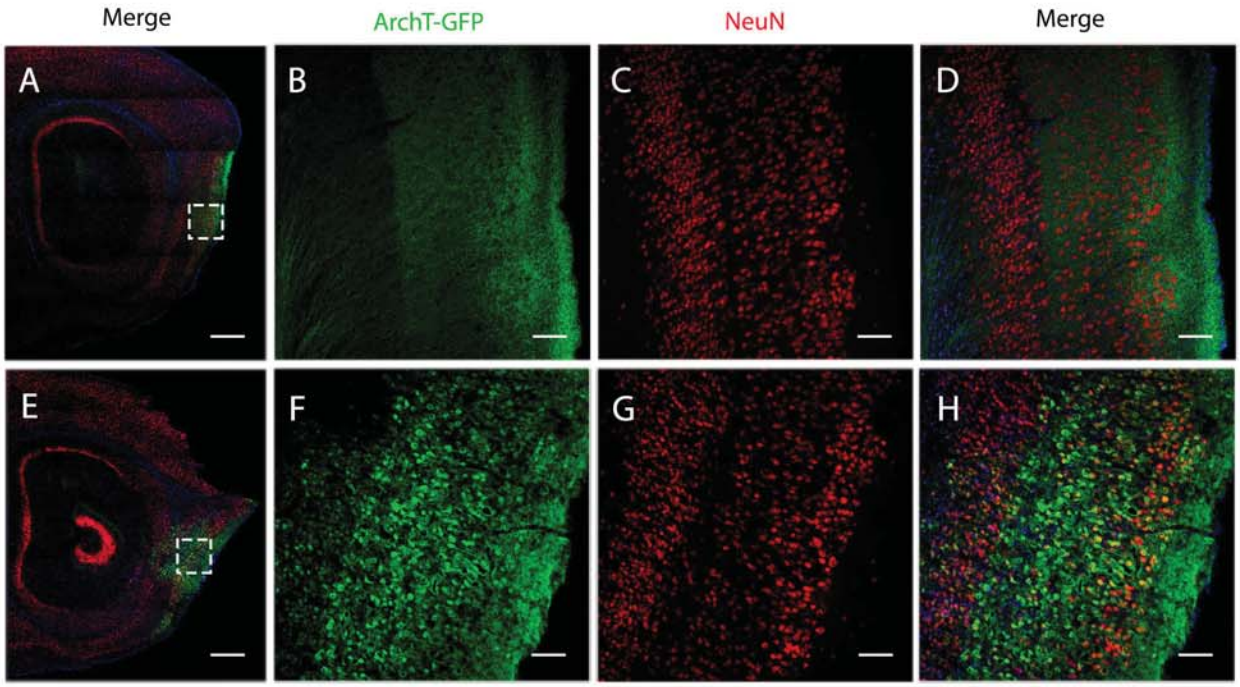

Supplemental figure 3

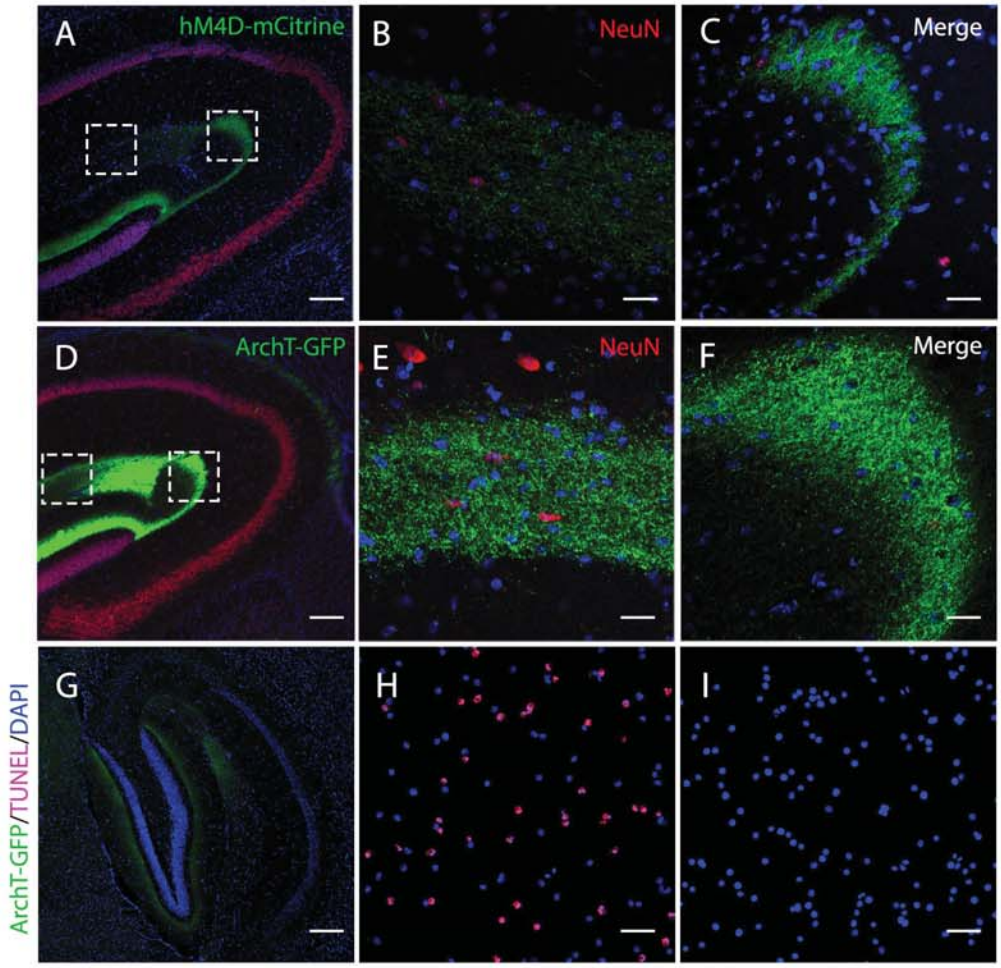

Supplemental figure 4

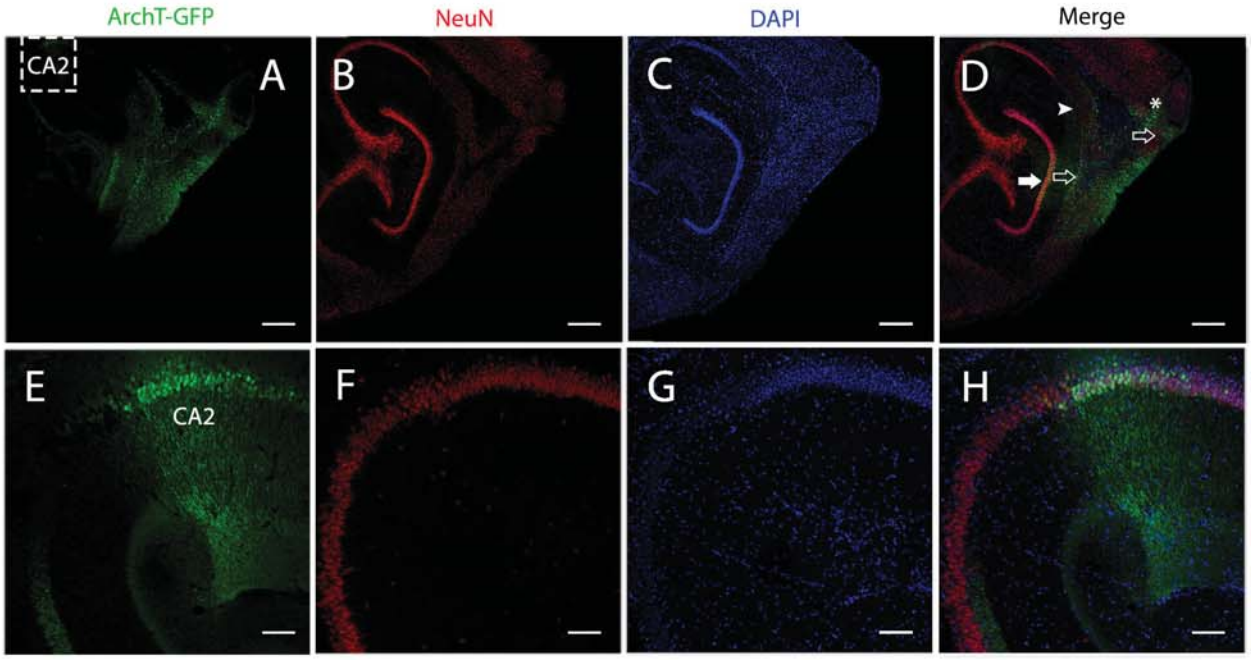

Supplemental figure 5

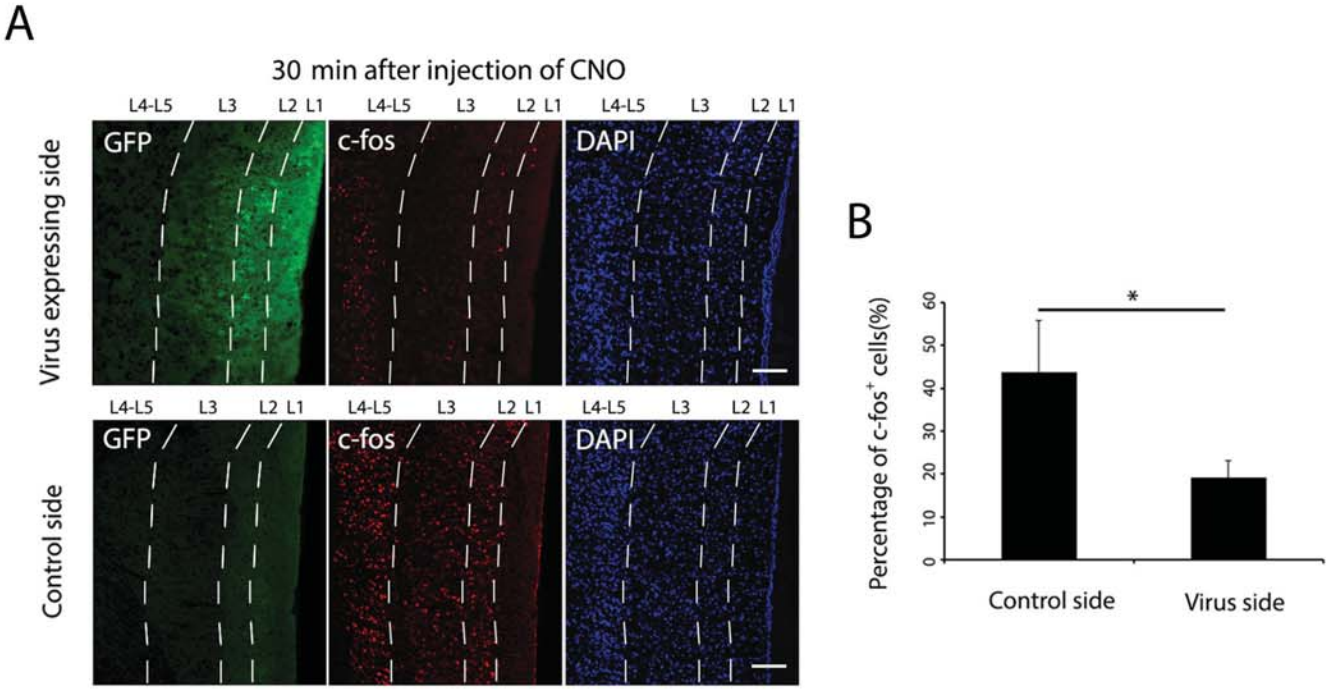

Supplemental figure 6

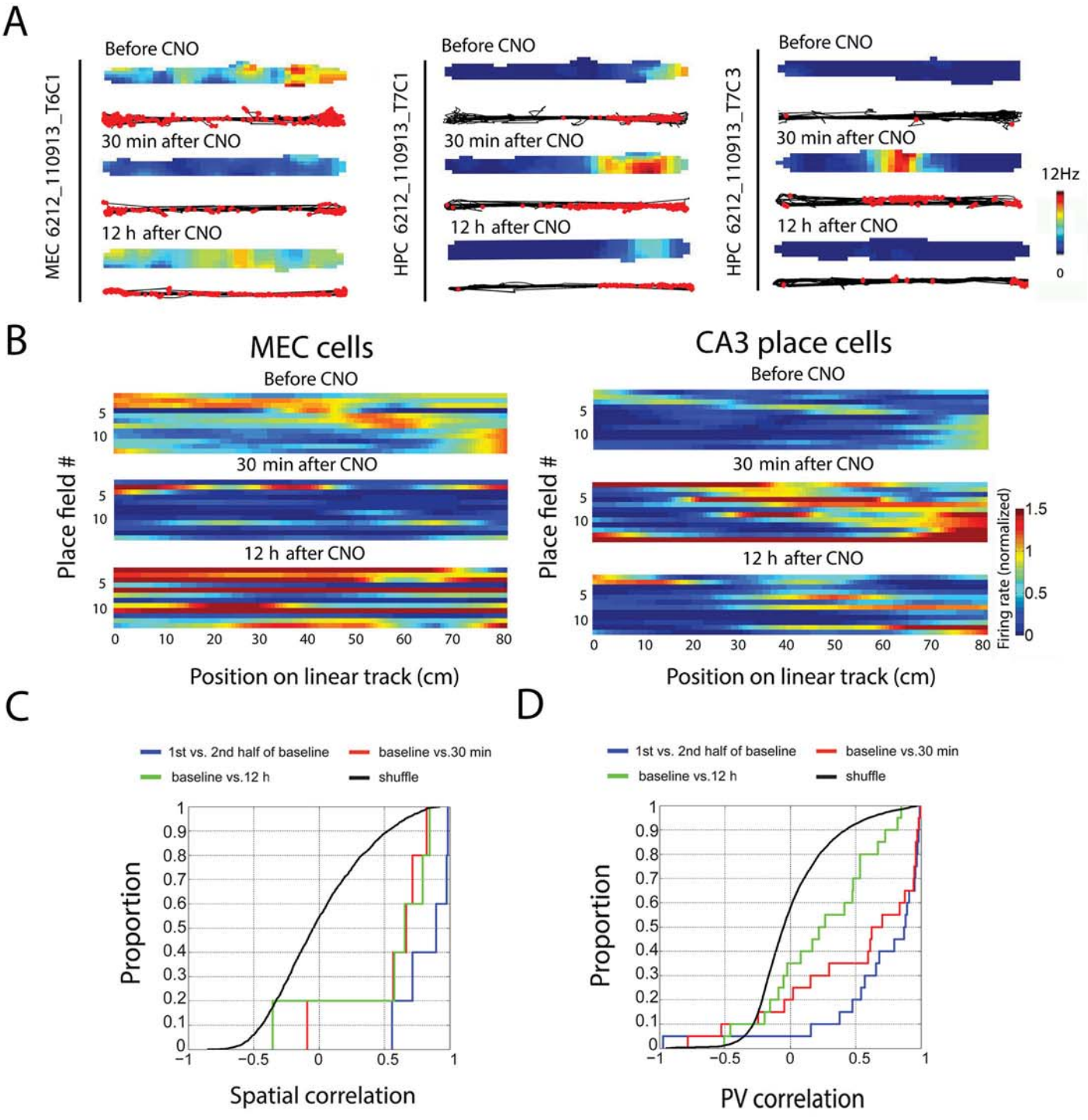

Supplemental figure 7

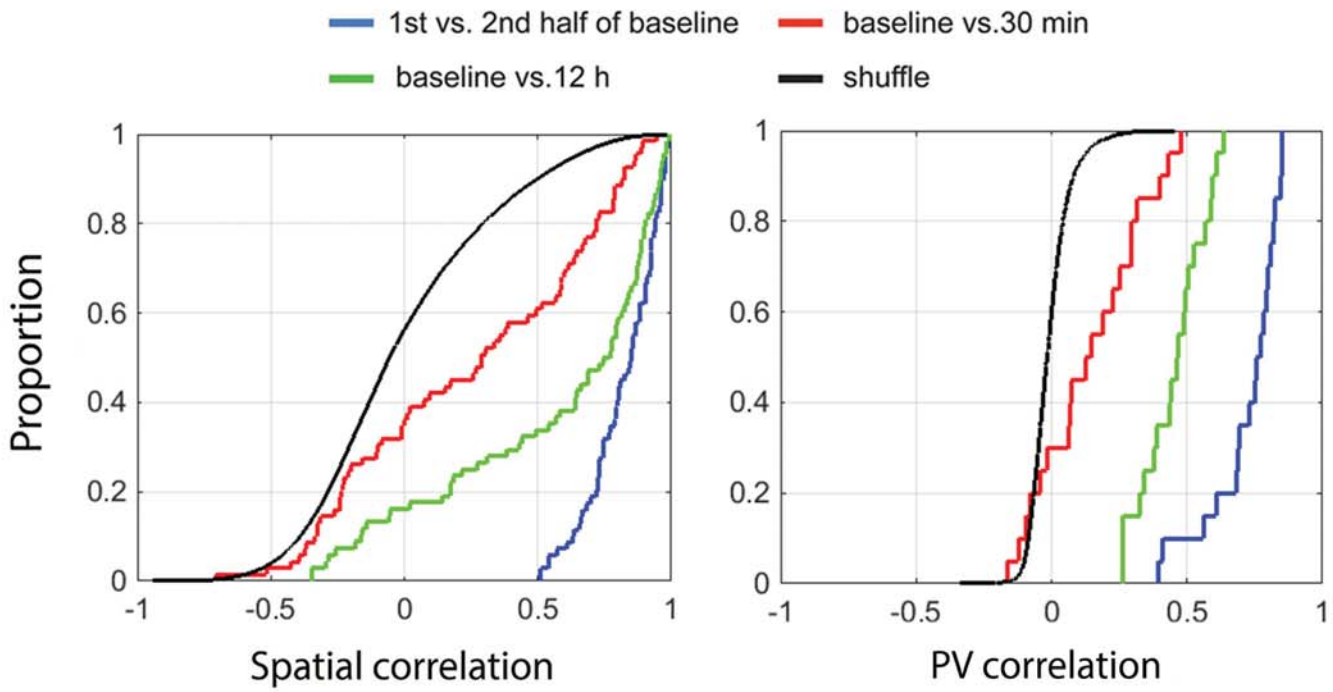

Supplemental Table 1

hM4D mouse #	infection of MEC[1]	infection outside of MEC[2]	infection of LEC[3]	infection of presubiculum[3]	infection of parasubiculum[3]	infection of postrhinal cortex[3]	infection of subiculum[3]	infection of dente gyrus[3]
1549	57.7%	19.9%	4.2%	9.6%	22.1%	16.7%	2.4%	0.8%
1742	60.3%	25.2%	10.0%	15.4%	18.3%	19.3%	4.8%	0.6%
1744	64.8%	11.0%	1.1%	3.5%	16.0%	8.6%	2.4%	0.0%
1550	25.9%	29.2%	0.0%	0%	14.5%	25.5%	0.0%	0.0%
1552	44.3%	16.4%	0.0%	9.8%	6.5%	10.2%	5.8%	0.3%
1875	23.1%	12.4%	6.7%	0.0%	2.2%	0.0%	0.0%	0.0%
1876	43.5%	16.0%	0.0%	2.6%	5.7%	15.2%	0.0%	0.0%
1866	28.5%	20.9%	8.7%	0.0%	0.0%	0.0%	0.0%	0.0%
1879	29.2%	32.0%	9.5%	14.1%	0.0%	0.0%	0.0%	0.0%
6210	43.2%	9.8%	0.0%	2.4%	0.0%	5.6%	0.0%	0.0%
6212	38.5%	11.1%	0.0%	3.7%	0.0%	6.8%	0.0%	0.0%
58008	61.9%	13.1%	9.6%	11.3%	20.8 %	42.6%	9.0%	0.0%
58009	78.3%	17.2%	7.8%	9.1%	16.1%	8.6%	0.1%	0.0%
52552	62.0%	12.8%	4.2%	11.3%	17.5%	13.4%	2.0%	0.7%
52553	57.8%	16.6%	2.4%	4.7%	18.6%	9.3%	0.0%	0.0%

ArchT mouse#	infection of MEC[1]	infection outside of MEC[2]	infection of LEC[3]	infection of presubiculum[3]	infection parasubiculum[3]	infection of postrhinal cortex[3]	infection of subiculum[3]	infection of dente gyrus[3]
1254	35.3%	9.0%	0.0%	0%	8.8%	2.4%	0%	0.0%
1544	39.1%	19.3%	0.0%	12.1%	6.5%	11.8%	0%	0.0%
1560	66.0%	16.1%	2.2%	9.8%	6.3%	8.1%	4.8%	0.0%
58012	53.0%	23.7%	5.8%	0%	18.4%	5.3%	5.2%	0.0%
52514	57.2%	32.0%	10.3%	2.0%	20.2%	2.6%	14.5%	0.0%
52558	70.4%	18.3%	3.8%	5.9%	19.8%	11.7%	0%	0.7%
58010	54.3%	26.7%	4.2%	4.6%	18.5%	18.3%	2.4%	0.0%
58011	53.3%	27.0%	7.3%	8.2%	13.1%	12.7%	3.1%	0.0%

1.Infection area / total MEC area; 2.Infection area in neighboring region of MEC / total infection area; 3.Infection area in the listed region / total area this region. LEC, lateral entorhinal cortex.

Supplemental Table 1. Percentage of area with mCitrine-expressing cells in specific parahippocampal regions for individual animals. Mice receiving AAV-hM4D and AAV-ArchT are shown separately in the upper and lower tables, respectively. Infection of MEC refers to the percentage of the surface area of MEC containing infected neurons. Infection outside of MEC refers to the percentage of the total infected area that was outside of MEC. Infection of lateral entorhinal cortex (LEC), pre- and parasubiculum, subiculum, dente gyrus and postrhinal cortex refers to percentages of the surface area of these regions in which infection was present. Note that in case of LEC, the percentage refers to the parts of LEC directly adjacent to MEC, present in sections that contained MEC.

Supplemental Table 2

hM4D mouse#	Spatial correlation			PV correlation		
	1st vs. 2nd half of baseline[1]	2nd vs. 1st session[1]	Statistic[3]	1st vs. 2nd half of baseline[2]	2nd vs. 1st session[2]	Statistic[4]
1550	1.26 ± 0.144	0.820 ± 0.267	t(11) = 2.43, P=0.0332	1.22 ± 0.085	0.566 ± 0.162	t(38) = 4.91, $P=1.76 \times 10^{-5}$
1552	0.98 ± 0.119	0.733 ± 0.224	t(9) = 1.58, P=0.149	0.727 ± 0.122	0.031 ± 0.110	t(38) = 5.06, $P=1.10 \times 10^{-5}$
52552	1.19 ± 0.116	0.145 ± 0.093	t(11) = 8.73 $P=2.82 \times 10^{-6}$	1.20 ± 0.145	0.207 ± 0.107	t(38) = 5.83, $P=9.70 \times 10^{-7}$
58008	1.03 ± 0.114	0.617 ± 0.183	t(8)= 2.22 P=0.057	1.08 ± 0.099	0.416 ± 0.129	t(38) = 3.96, $P=3.18 \times 10^{-4}$
58009	1.02 ± 0.129	0.847 ± 0.270	t(7)= 0.795 P=0.453	1.09 ± 0.109	0.748 ± 0.062	t(38) = 2.02, P=0.05

ArchT Mouse#	Spatial correlation			PV correlation		
	1st vs. 2nd half of baseline[1]	2nd vs. 1st session[1]	P value Statistic[3]	1st vs. 2nd half of baseline[2]	2nd vs. 1st session[2]	Statistic[4]
1254	1.04 ± 0.123	0.670 ± 0.212	t(10) = 1.968 P=0.077	0.448 ± 0.081	0.278 ± 0.097	t(38) = 1.67, P=0.104
2198	1.15 ± 0.130	0.523 ± 0.196	t(11) = 3.85 P=0.0027	0.815 ± 0.088	0.426 ± 0.120	t(38) = 2.90, P=0.0062
58011	1.43 ± 0.080	0.289 ± 0.086	t(38) = 7.92 $P=1.47 \times 10^{-9}$	1.00 ± 0.105	0.091 ± 0.055	t(38) = 7.56, $P=4.29 \times 10^{-9}$

1. Spatial correlation with Fisher z-transformation; 2. Population vector correlation with Fisher z-transformation; 3. Spatial correlation of the 2nd vs. 1st session compared with spatial correlation of the 1st vs. 2nd half of the 1st session; 4. Population vector correlation of the 2nd vs. 1st session compared to the population vector correlation of the 1st vs. 2nd half of the 1st session.

Supplemental Table 2. Change in spatial correlation and population vector (PV) correlation after silencing of MEC input for individual animals with 8 stable place fields or more. Mice receiving AAV-hM4D or AAV-ArchT are shown separately (upper and lower tables, respectively). Spatial correlations and PV correlations from individual animals were Fisher z-transformed to approach a normal distribution. 1st session is the baseline session; 2nd session begins 30 min after CNO; 3rd session begins 12 h after CNO. Spatial correlations and PV correlations were computed for the 1st half vs. 2nd half of the 1st session, and for the 1st vs. the 2nd session. A paired-sample t test was performed to assess the change of spatial correlations. An independent sample t test was used for the comparison of PV correlations on the track.

Group	Spatial correlation			PV correlation		
	1st vs. 2nd half of baseline[1]	2nd vs. 1st session[1]	Statistic[3]	1st vs. 2nd half of baseline[2]	2nd vs. 1st session[2]	Statistic[4]
hM4D	1.10 ± 0.054	0.57 ± 0.184	t(4) = 3.32, P=0.029	1.06 ± 0.089	0.394 ± 0.127	t(4) = 6.55, P=0.003
ArchT	1.21 ± 0.114	0.494 ± 0.111	t(2) = 3,162, P=0.087	0.755 ± 0.163	0.265 ± 0.097	t(2) = 2.22, P= 0.156

1. Spatial correlation with Fisher z-transformation; 2. Population vector correlation with Fisher z-transformation; 3. Spatial correlation of the 2nd vs. 1st session compared with spatial correlation of the 1st vs. 2nd half of the 1st session; 4. Population vector correlation of the 2nd vs. 1st session compared to the population vector correlation of the 1st vs. 2nd half of the 1st session.

Supplemental Table 3. Mean spatial correlation and population-vector correlation using means for individual animals as data points. Mice receiving AAV-hM4D or AAV-ArchT are shown separately (upper and lower rows, respectively). Conventional t-tests were used to compare baseline and inactivation trials, as well as the first and the second half of the baseline trial. It can be seen that correlations between baseline and inactivation trials are significantly lower than between blocks of the baseline trial also when only one data point is used per animal.

Group	Spatial correlation			PV correlation		
	1st vs. 2nd half of baseline[1]	2nd vs. 1st session[1]	Statistic[3]	1st vs. 2nd half of baseline[2]	2nd vs. 1st session[2]	Statistic[4]
hM4D	1.10 ± 0.047	0.51 ± 0.083	$t(81) = 6.87$, $P=1.17 \times 10^{-9}$	0.828 ± 0.034	0.337 ± 0.044	$t(38) = 8.80$, $P=1.04\times 10^{-10}$
ArchT	1.29 ± 0.054	0.445 ± 0.074	$t(80) = 9.06$, $P=5.51 \times 10^{-14}$	0.967 ± 0.048	0.211 ± 0.0345	$t(38) = 12.8$, $P=2.55 \times 10^{-15}$

1. Spatial correlation with Fisher z-transformation; 2. Population vector correlation with Fisher z-transformation; 3. Spatial correlation of the 2nd vs. 1st session compared with spatial correlation of the 1st vs. 2nd half of the 1st session. 4. Population vector correlation of the 2nd vs. 1st session compared to the population vector correlation of the 1st vs. 2nd half of the 1st session.

Supplemental Table 4. Change in spatial correlation and population vector (PV) correlation after silencing of MEC input for animals without any infection in the dentate gyrus. Mice receiving AAV-hM4D or AAV-ArchT are shown separately (upper and lower rows, respectively). Spatial correlations and PV correlations from individual animals were Fisher z-transformation to approach a normal distribution. 1st session is the baseline session; 2nd session begins 30 min after CNO. Spatial correlations and PV correlations were computed for the 1st half vs. 2nd half of the 1st session, and for the 1st vs. the 2nd session. A paired-sample t test was performed to assess the change of spatial correlations. An independent sample t test was used for the comparison of PV correlations on the track.

Group	Spatial correlation			PV correlation		
	1st vs. 2nd half of baseline[1]	2nd vs. 1st session[1]	Statistic[3]	1st vs. 2nd half of baseline[2]	2nd vs. 1st session[2]	Statistic[4]
hM4D	1.16 ± 0.053	0.59 ± 0.078	t(148) = 6.00, $P=1.47 \times 10^{-8}$	0.858 ± 0.028	0.172 ± 0.028	t(38) = 17.2, $P=1.73 \times 10^{-19}$
ArchT	1.15 ± 0.055	0.487 ± 0.088	t(110) = 6.09, $P=1.77 \times 10^{-8}$	0.967 ± 0.048	0.245 ± 0.044	t(38) = 11.0, $P= 2.15 \times 10^{-13}$

1. Spatial correlation with Fisher z-transformation; 2. Population vector correlation with Fisher z-transformation; 3. Spatial correlation of the 1st vs. 2nd half of the 1st session cross cells after considering only one running direction; 4. Population vector correlation of the 2nd vs. 1st session compared to the population vector correlation of the 1st vs. 2nd half of the 1st session after considering only one running direction.

Supplemental Table 5. Mean spatial correlation and population-vector correlation when only one running direction is considered. When a cell had a stable place field in one running direction only, this direction was chosen. When stable fields were detected in both directions, one of the directions was chosen randomly. Mice receiving AAV-hM4D or AAV-ArchT are shown separately (upper and lower rows, respectively). It can be seen that correlations between baseline and inactivation trials are significantly lower than between blocks of the baseline trial also when only one running direction is analyzed.